

Louisiana State University

## LSU Scholarly Repository

---

LSU Master's Theses

Graduate School

---

2011

### Boron and Rare Earth Oxide Composite Nanoparticles for Enhancement of Combustion

Jacob Hanberry

*Louisiana State University and Agricultural and Mechanical College*

Follow this and additional works at: [https://repository.lsu.edu/gradschool\\_theses](https://repository.lsu.edu/gradschool_theses)



Part of the [Chemical Engineering Commons](#)

---

#### Recommended Citation

Hanberry, Jacob, "Boron and Rare Earth Oxide Composite Nanoparticles for Enhancement of Combustion" (2011). *LSU Master's Theses*. 3367.

[https://repository.lsu.edu/gradschool\\_theses/3367](https://repository.lsu.edu/gradschool_theses/3367)

This Thesis is brought to you for free and open access by the Graduate School at LSU Scholarly Repository. It has been accepted for inclusion in LSU Master's Theses by an authorized graduate school editor of LSU Scholarly Repository. For more information, please contact [gradetd@lsu.edu](mailto:gradetd@lsu.edu).

# **BORON AND RARE EARTH OXIDE COMPOSITE NANOPARTICLES FOR ENHANCEMENT OF COMBUSTION**

A Thesis,

Submitted to the Graduate Faculty of the  
Louisiana State University and  
Agricultural and Mechanical College  
in partial fulfillment of the  
requirements for the degree of  
Master of Science in Chemical Engineering

In

The Department of Chemical Engineering

by

Jacob Hanberry  
B.S., Millsaps College, 2009  
August, 2011

## **ACKNOWLEDGEMENTS**

I would like to thank Dr. Kerry Dooley, my advisor, for his vast knowledge and continued guidance throughout this project. I would also like to thank Dr. Sumanta Acharya and Srinibas Karmakar for their collaboration and combustion work, and Dr. Amitava Roy and Dr. Dongmei Cao for their assistance with XRD work at CAMD and MCC, respectively. Thanks to The Office of Naval Research (ONR) [Contract# N00014-10-1-0276] for providing financial support. I would lastly like to thank my wife, Katie Hanberry, and two sons, Carter and Camden, for their continued support throughout my educational career.

# TABLE OF CONTENTS

ACKNOWLEDGEMENTS.....	ii
LIST OF TABLES.....	iv
LIST OF FIGURES.....	v
ABSTRACT.....	vii
CHAPTER 1: INTRODUCTION AND REVIEW OF LITERATURE.....	1
1.1 Introduction and Project Goals.....	1
1.2 Energetic Additives – Boron.....	2
1.3 Non-Energetic Oxide Additives .....	9
1.4 Mixed Metal and Metal/Oxide Syntheses.....	11
1.5 Mixed Metal and Metal/Oxide Combustion Studies.....	16
CHAPTER 2: EXPERIMENTAL PROCEDURES.....	18
2.1 Particle Preparation.....	18
2.2 Particle Characterization.....	19
2.3 Combustion Setup and Particle Collection.....	22
2.4 Exhaust Gas Analysis.....	24
CHAPTER 3: RESULTS AND DISCUSSION.....	26
3.1 Initial Particle Size, Structure and Composition.....	26
3.2 Boron Nanoparticles - Performance in Combustor.....	37
3.3 Final Particle Size, Structure, and Composition.....	44
CHAPTER 4: CONCLUSION.....	49
REFERENCES.....	51
APPENDIX A – GAS CHROMATOGRAPHY (GC) DETAILS.....	55
APPENDIX B – XRD DIFFRACTOGRAMS.....	56
VITA.....	64

## LIST OF TABLES

Table 2.1: T.C. response factors.....	25
Table 3.1: Scherrer calculations for SB99 and SB86, two boron phases.....	28
Table 3.2: Particle characteristics determined from N <sub>2</sub> adsorption-desorption measurements...31	
Table 3.3: Active particle contents and maximum oxidation temperature from TGA measurements in air.....	34
Table 3.4: ICP results for magnesium content.....	37
Table 3.5: Exhaust gas compositions case 1.....	41
Table 3.6: Exhaust gas compositions case 2.....	41
Table 3.7: Exhaust gas compositions case 3.....	42
Table 3.8: Burnt particle size estimates using the Scherrer equation.....	45
Table A1: GC settings.....	55
Table A2: GC retention times.....	55

## LIST OF FIGURES

Figure 1.1: Heating values of various metals and ethanol.....	4
Figure 2.1: Combustion apparatus.....	23
Figure 2.2: Particle Injection System.....	23
Figure 3.1: X-Ray diffractograms of SB99 and SB86.....	26
Figure 3.2: X-Ray diffractograms of Sintered, BM, BR41-1, and BR41-2.....	27
Figure 3.3: X-Ray diffractogram of BR41-1 collected at CAMD.....	28
Figure 3.4: SEM images of SB99 and SB86.....	29
Figure 3.5: SEM images of BM and Sintered.....	30
Figure 3.6: SEM images of BR41-1 and BR41-2.....	30
Figure 3.7: Cumulative pore volume distribution as computed by the BJH desorption method...	33
Figure 3.8: Normalized pore size distribution as a function of pore diameter.....	33
Figure 3.9: TGA analysis in air for boron and boron/REO nanoparticles.....	35
Figure 3.10: Derivative TGA for boron and boron/REO nanoparticles.....	36
Figure 3.11: Temperature data for SB99, SB86, and BM at exit (20 in. above dump plane).....	38
Figure 3.12: Temperature data for Sintered, BR41-1, and BR41-2 at exit (20 in. above dump plane).....	39
Figure 3.13: Temperature data for SB99 and SB86 15 in. above the dump plane.....	39
Figure 3.14: X-Ray diffractograms of burnt SB99 and Sintered.....	45
Figure 3.15: SEM images of collected burnt SB99.....	46
Figure 3.16: SEM images of collected burnt SB86.....	46
Figure 3.17: TGA results in air, collected burnt particles.....	47
Figure 3.18: Derivative TGA for collected burnt particles.....	48
Figure A1: X-Ray diffractogram of SB99.....	56

Figure A2: X-Ray diffractogram of SB86.....	56
Figure A3: X-Ray diffractogram of BM.....	57
Figure A4: X-Ray diffractogram of Sintered.....	57
Figure A5: X-Ray diffractogram of BR41-1.....	58
Figure A6: X-Ray diffractogram of BR41-2.....	58
Figure A7: X-Ray diffractogram of SB99 (CAMD).....	59
Figure A8: X-Ray diffractogram of SB86 (CAMD).....	59
Figure A9: X-Ray diffractogram of BR41-1 (CAMD).....	60
Figure A10: X-Ray diffractogram of SB99 burnt.....	61
Figure A11: X-Ray diffractogram of SB86 burnt.....	61
Figure A12: X-Ray diffractogram of BM burnt.....	62
Figure A13: X-Ray diffractogram of Sintered burnt.....	62
Figure A14: X-Ray diffractogram of BR41-1 burnt.....	63
Figure A15: X-Ray diffractogram of BR41-2 burnt.....	63

## ABSTRACT

Metallic fuels are of interest as additives in bio-fuel combustion because of their high heating values, and this thesis deals with the experimental investigation of boron nanoparticles and their effect on ethanol combustion. Two grades of boron nanoparticles were commercially purchased and modified to obtain different physical characteristics, by ball milling and sintering. Also, a mixture of rare-earth oxide ( $\text{CeO}_2$ ,  $\text{La}_2\text{O}_3$ , and  $\text{Gd}_2\text{O}_3$ ) nanoparticles was synthesized and added to the boron nanoparticles in varying amounts to form composite mixtures. The effects of rare-earth oxides on boron combustion were investigated using these composites.

Particle characterizations were carried out by X-ray diffraction, scanning electron microscopy, porosimetry, and thermogravimetric analysis. Nanoparticles were characterized by crystallinity, primary particle size, agglomerate size, and the elemental (zero valent) boron content, both pre- and post-combustion. Exhaust gas chromatographic analysis and temperature measurements in the post-flame region of the combustion unit were carried out in order to determine the particles' effects on combustion.

Commercial boron nanoparticles of different grades differ in agglomerate size, but the primary nanoparticle sizes are similar,  $\sim 70$  nm. The agglomerate size can be modified by ball milling, while the primary nanoparticle size can be increased by high-temperature calcination. The combustion data suggest that the addition of boron nanoparticles to an ethanol fuel increases both the overall temperature of the system and the production of  $\text{CO}_2$ , and adding rare-earth oxides to boron nanoparticles can also enhance these measures of performance. The data also suggest that as the boron primary particle size and agglomeration decrease, boron nanoparticles have a greater positive impact on ethanol combustion.



# CHAPTER 1

## INTRODUCTION AND REVIEW OF LITERATURE

### 1.1 Introduction and Project Goals

The depletion of fossil fuels and concerns over greenhouse gas emissions have been the motivation for finding alternative energy sources. Possible candidates for alternative energy sources include bio-fuels, wind, solar, geothermal, and hydro(tidal) energies. The renewability of these energy sources makes them good candidates. Petroleum based non-renewable fuels provide the majority of the world's energy and are becoming more costly. The amount of energy consumed from petroleum based fuels accounts for 40% of the world's use, while renewable sources account for 6% (Demirbas, 2007). Replacing such a large portion of energy usage would take a combined effort to develop many different alternative sources, including bio-fuels.

Bio-fuels are those derived from biomass, and can be solid, liquid, or gaseous (Demirbas, 2007). Of particular interest are liquid bio-fuels such as ethanol, because they can replace petroleum based fuels in internal combustion engines. Current technology allows vehicles to run on up to 85% ethanol in E85 flex fuel vehicles. One of the major drawbacks of using ethanol and similar bio-fuels is that their energy densities are much lower than typical petroleum based fuels such as, 21 kJ/mL for ethanol versus 30-35 kJ/mL for gasoline and diesel. One way to help combat this energy deficiency in bio-fuel systems is to add energetic metal particles as fuel additives. Such metal particles are of interest in part because they release large amounts of heat upon burning, thereby aiding in ignition. Some drawbacks with metal fuels are that they tend to partially oxidize at very mild conditions (in handling, e.g.) and yet can be difficult to completely burn due to transport limitations through the oxide layer. An even larger drawback is lack of recyclability; there are no ways at present to easily regenerate (reduce back to the zero valent

state) the metal particles for reuse. While this is not a problem in certain specialty combustion applications (e.g., Ramjets), it could limit the use of metal particle-aided combustion in larger volume power-plant applications.

Research has shown some promise in overcoming these barriers, and this project deals with boron/ethanol combustion. The main goal is to study the effects of boron nanoparticles on ethanol combustion. It is possible that use of nano- rather than micron-sized particles in a standard spray/swirl vane combustion apparatus might result in more complete combustion of the boron, and therefore have more of an effect on the liquid fuel combustion. It is also possible that, if the particles do not agglomerate during combustion, they may be easier to regenerate.

Therefore it is desired to determine how boron particle size, composition, and agglomeration at the nano-scale affects combustion and heat release using a typical bio-fuel, ethanol. Boron nanoparticles and mixtures of elemental boron and rare-earth oxide nanoparticles have been studied with the goal of enhancing the combustion of both the ethanol and the boron itself. All particles used (pre- and post-combustion) have been characterized for size, agglomeration, crystal structure, surface area, and elemental boron content in order to obtain a better understanding of the effects of particle morphology and surface chemistry.

## **1.2 Energetic Additives - Boron**

The use of metal particles as fuel additives is of interest due to the high heating values of such metals. Aluminum, boron, beryllium, tungsten, titanium, etc. are some of the metal powders which have been considered. Figure 1.1 shows both gravimetric and volumetric heating values for various metals and ethanol. It is seen that the metals have considerably higher heating values than ethanol. Boron and beryllium also show considerably higher energies on a volumetric basis,

and this makes them of particular interest for volume-limited systems (Kuo et al., 2003). Theoretical calculations of heat evolution have shown that additions of boron and aluminum to hydrocarbon fuels can increase the overall heat release of hydrocarbon fuels (Goroshin et al., 2001). One problem associated with using such metal particles is that they often have a native oxide layer on the surface after handling in the atmosphere. This makes combustion more difficult, because now either the  $O_2$  or the boron must diffuse through the oxide layer, which could be a liquid or a non-porous solid. The presence of an oxide layer also causes higher ignition temperatures (Yetter et al., 2009). Because of this, it is of interest to synthesize particles that either do not have an oxide layer, or whose oxide layer is porous enough to easily transport oxygen, or which conducts oxygen in the form of oxide ions easily at high temperature.

Some work has been done to disperse metal particles in hydrocarbons to protect the pure particles from oxide layer formation. In particular, Van Denever et al. (2009) demonstrated that the use of oleic acid surfactant protected boron from surface oxidation to a degree undetectable by XPS measurements.

Another problem associated with metal nanoparticles is their agglomeration. In ball-milling techniques, Van Denever et al. (2009) used a suspending solvent of hexane to prevent agglomeration during particle synthesis. Singhal et al. (1999) showed that in a chemical vapor condensation synthesis of  $TiO_2$  and  $Al_2O_3$  nanoparticles above 573 K, agglomeration is unavoidable and a primary particle size of 15-20 nm resulted in approximately 100 nm aggregates. They suggested agglomeration may be controlled by residence time and precursor concentrations. No work has shown any differences in agglomeration between micron-sized particles and nanoparticles.

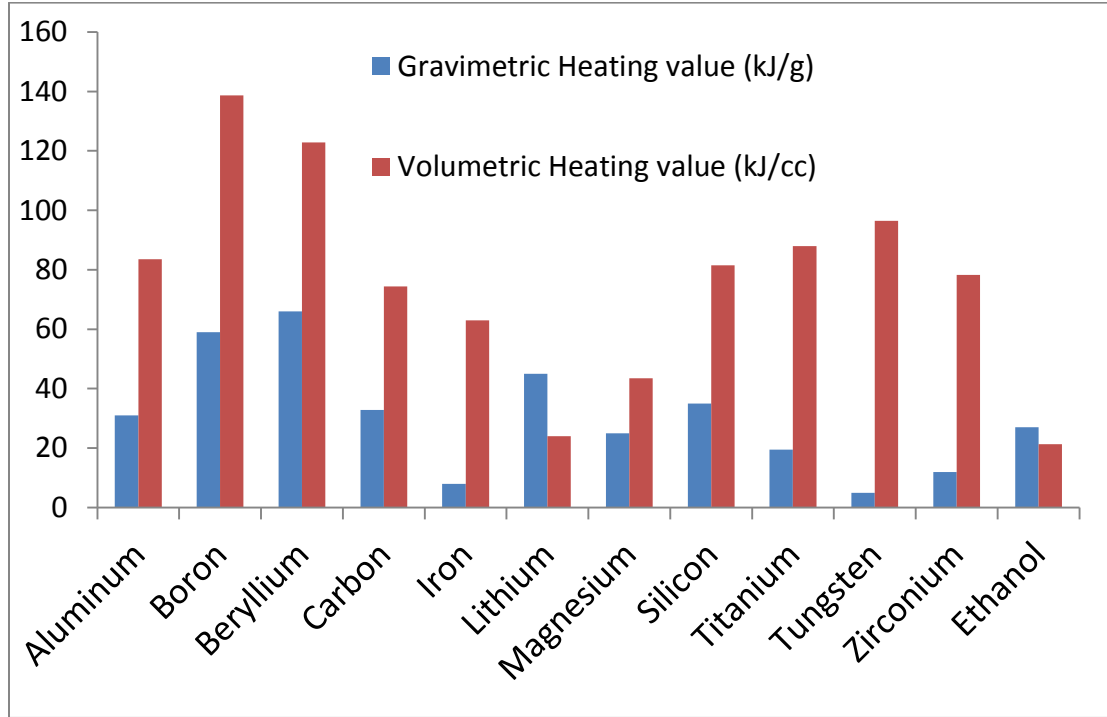


**Figure 1.1: Heating values of various metals and ethanol (Karmakar, 2011).**

Nano-sized particles exhibit significantly different physical properties from their chemically similar particles of larger size (Yetter et al., 2009), most notably higher surface area, lower melting points, and in some cases enhanced catalytic activity. Dreizin et al. (2009) summarized the preparation of Al, Ti, Mg, B, Ni, and Zr nanoparticles by powder mixing, sol-gel techniques, self-assembly, deposition methods, and reactive milling. In a micellar template-assisted self assembly, Mehendale et al. (2006) successfully prepared 80 nm  $\text{Fe}_2\text{O}_3$  and Al particles. Schoenitz et al. (2005) demonstrated reactive milling as a successful synthesis technique for Al- $\text{Fe}_2\text{O}_3$  and Al- $\text{MoO}_3$  metal particles in the range of 30-50 microns and proposed the synthesis conditions had no effect on particle size, stating that particle size is strictly dependent on the size of the unmilled materials. Nanoparticle suspensions (low concentrations), higher concentration gels, and solid fuels are some of the ways nanoparticles can be used in

systems (Yetter et al., 2009). Solid nanoparticles are produced industrially and so most studies have made use of such particles.

As mentioned previously, boron's high heating values make it a desirable fuel additive, but combustion of boron particles can be slow due to a native oxide layer on the surface. Widely varying ignition temperatures for boron combustion have been reported: 800-1100 K for particle agglomerates (Shevchuk et al., 1975), 1400-1600 K for 3-12  $\mu\text{m}$  particles suspended in gas (Zolotko et al., 1977), and 1850-1950 K for single 35-45  $\mu\text{m}$  particles (Macek et al., 1969). It has been shown that ignition temperatures decrease with decreasing particle size (Ashish et al., 2010).

Early on, Macek et al. (1969) described boron combustion as a two stage process. The first stage is the removal of the surface oxide layer (ignition), and the second stage is the burning of pure boron (combustion). The limiting step in combustion is presumably removing the oxide layer. The melting point of the oxide (723 K) is much lower than that of boron (>2500 K); therefore, at combustion temperatures the solid boron core can be covered by a molten shell of  $\text{B}_2\text{O}_3$ . No work exists to support or refute the claim that the oxide wets the surface, but the modeling and experimental studies mentioned in this review assume the oxide completely entraps the core. Two different processes have been proposed for transport through the oxide. King (1974) proposed that the oxide layer melts and  $\text{O}_2$  dissolves in it to reach the boron core, where combustion takes place. In contrast, Li and Williams (1988) and Glassman (1984) proposed that boron dissolves and diffuses through the molten layer until it reaches the  $\text{B}_2\text{O}_3$ /air interface where oxidation occurs. In both cases, the process is limited by diffusion through the molten  $\text{B}_2\text{O}_3$  layer.

Yeh et al. (1996) proposed that the heat released from the heterogeneous reaction of B(s) and O<sub>2</sub>(g) supplies the heat needed to vaporize B<sub>2</sub>O<sub>3</sub> and “peel” the oxide layer away. Once this layer is vaporized, the combustion stage takes over and pure boron is burnt rapidly. Gany (2006) thermodynamically modeled the combustion of 60%B/40%HTPB (hydroxyl-terminated-polybutadiene) and found that below an equivalence ratio of 0.7, the actual vapor pressure of B<sub>2</sub>O<sub>3</sub> is higher than its equilibrium pressure and the shell is completely vaporized. Above the equivalence ratio of 0.7, the equilibrium pressure of B<sub>2</sub>O<sub>3</sub> is above its vapor pressure and the molten oxide cannot be completely removed. Brown et al. (1991) modeled the gasification of the oxide layer using bond energies and transition state arguments to propose that in particles with diameters >200μm, the process is diffusion limited, and in particles with diameter 50-200μm, the process is kinetically limited and directly proportional to particle size. Their model also showed that in the presence of hydrocarbons, surface reactions with OH radicals and H<sub>2</sub>O significantly increased the gasification rate. Driezen et al. (1995) proposed that the simultaneous dissolution of boron and oxygen into the molten B<sub>2</sub>O<sub>3</sub> shell react to form BO complexes, and oxygen continually dissolves in the molten layer until it becomes saturated, leading to rapid combustion. The former case is limited by the surface reactions with the oxide, while the latter is limited by the dissolution of O<sub>2</sub> in the molten layer. In a combustion experiment of various nitrogen-oxidizer mixtures and boron particles 75-200 μm, Gurevich et al. (1969) tracked particles with a 35 mm camera and concluded that the rate of removal of the oxide layer (ignition) decreased with increasing particle size and increased with increasing water content. A 50% increase in particle size more than doubled the ignition time, while an 11% increase in water content reduced the ignition time by ~25%.

Theoretical kinetics and thermodynamic models have been postulated to better understand the combustion process. Yetter et al. (1991) modeled the B/O/H/C gas-phase system at high temperatures using thermodynamic parameters and assuming quasi-equilibrium kinetics in the gas phase, with JP4 as the fuel source from 1600-2000 K, and found that above 1600 K in oxygen-rich environments the dominant species are HOBO and B<sub>2</sub>O<sub>3</sub>. In fuel-rich combustion, the dominant species are HBO, BO, and B<sub>2</sub>O<sub>2</sub>, with HOBO and B<sub>2</sub>O<sub>3</sub> concentrations three orders of magnitude smaller. Brown et al. (1993) proposed similar mechanisms for the surface reactions by kinetics analysis using transition state theory in hydrocarbon/boron combustion, but concluded that the major product is HOBO. They also proposed that in an oxygen-rich environment the major products are HOBO, B<sub>2</sub>O<sub>3</sub>, and BO<sub>2</sub>, while in fuel-rich environments they are HBO, B<sub>2</sub>O<sub>2</sub> and BO. Theoretical models based on transition state theory have shown that gaseous HOBO reacts to B<sub>2</sub>O<sub>3</sub> during cooling (Slutskii et al., 1997); therefore, the only way to detect HOBO as a combustion product is to measure gas phase compositions in-situ, and no known work has done so. Therefore the models show that at actual combustion temperatures HOBO and similar suboxides are the major products in hydrocarbon combustion environments, which reduces the heat release of the boron combustion in the hydrocarbon combustion zone.

Different experimental studies have tried to confirm or rebut these models. Macek et al. (1969) studied the combustion of single boron particles of 30-45  $\mu\text{m}$  at atmospheric conditions by time exposure microphotography in a laminar flow burner gas consisting of propane and oxygen. They observed two separate regions of burning, which they denoted ignition and combustion. They measured ignition temperatures of 1850-2000 K, depending on the gaseous atmosphere, with wet atmospheres decreasing the ignition temperature. The burning rates increased with increasing amounts of O<sub>2</sub>. Li et al. (1988) also observed separate regions of

ignition and combustion spectroscopically, injecting  $\sim 1\ \mu\text{m}$  particles into a flat flame burner with methane and oxygen. They distinguished a bright yellow region as ignition and a green region as combustion, with the most abundant wavelength (5420 nm) indicative of  $\text{BO}_2$ . The ignition process was rate limiting. Ulas et al. (2001) studied methane/boron combustion in various mixtures of  $\text{NF}_3/\text{N}_2/\text{O}_2$  oxidizers with a CCD camera and noted similar two-stage combustion, with ignition being the limiting step. With fluorine in the oxidizing mixture, they did not see two-stage combustion and believed this to be due to the rapid removal of the oxide layer by fluorine.

In a study of combustion of single boron particles ranging from 75-200  $\mu\text{m}$ , Gurevich et al. (1969) found that the ignition temperature of amorphous agglomerates was lower than that of solid crystalline particles, and they determined that after combustion, it was possible to collect burnt products that were a factor of 2-20 times smaller than the feed particles. This is of particular relevance to the regeneration of nano-sized combustion products. Other work has confirmed the reports of amorphous boron igniting faster than crystalline particles (Mohan et al., 1972). Yeh et al. (1996) studied the ignition and combustion of 1-3  $\mu\text{m}$  boron particles in methane/oxygen in a flat flame burner, and found ignition times for amorphous particles to be 0.04 ms shorter than for crystalline particles of the same size. Total burn time decreased by 0.17 ms for amorphous particles.

The previous studies showed that ignition times and combustion of micron-sized particles are dependent on particle size, crystallinity, and combustion environment, but some recent work has been done using nano-sized particles. Young et al. (2009) studied the combustion of 60 nm boron nanoparticles in methane/air, and found the ignition times ranged from 1.5 to 6 ms at mole fractions of oxygen from 0.1-0.3 and temperatures 1580-1810K. Ignition times here are similar



to ignition times reported Yeh et al. (1996) for micron-sized particles which also ranged from 1.5 to 6 ms. They noted that the ignition times were insensitive to oxygen mole fraction but dependent on temperature. They also found that the second stage of combustion was similar to that of 1-3  $\mu\text{m}$  particles, and concluded that agglomeration of the nanoparticles (during preparation) was the cause of longer burning times. Sullivan et al. (2009) studied 30-90 mol%B Al/B composite nanoparticles ( $\sim 60$  nm) in a batch combustion cell by timed pressure change with CuO as the oxidizer, and found that the reactivity of the composites increased with increasing boron content until about 50 mol%, from which point reactivity decreased rapidly. So while not much work has been published on boron nanoparticles as fuel additives, the preliminary data suggest that it is definitely an area worthy of further research. Other ways to overcome the slow ignition and incomplete combustion of boron might be to alloy or mix it with other more combustible metals, or with a non-combustible catalyst for the boron or fuel (or both) oxidation.

### **1.3 Non-Energetic Oxide Additives**

By this term it is meant that a metal oxide is used as a fuel additive. Such additives have long been of interest for catalytic purposes, or for reducing unwanted emissions such as  $\text{NO}_x$  or CO. They could also function to control deposits, eliminate knocking, and lead to more complete combustion through catalytic oxidation of CO (Rang et al., 2003). Many different additives have been studied for their abilities to fulfill one of the tasks mentioned above. The goal here is to catalytically enhance combustion, and so this review focuses on additives that could serve this purpose. Alkali and alkali earth metal derivatives, organometallic compounds, metal oxides, peroxides, and hydroxides have been reviewed as possible fuel additives by Rang et al. (2003). Rare-earth metals and their oxides are known to be effective combustion catalysts in a wide array

of applications. Cerium oxide, in particular, has been known to function as a combustion catalyst due to its ability to cycle between the oxidized ( $\text{Ce}^{4+}$ ) and reduced ( $\text{Ce}^{3+}$ ) states readily, and to store and donate oxygen (Trovallaleli et al., 1999; Cordatos et al., 1996; Aneggi et al., 2006).

These characteristics have led to cerium oxide being effective in exhaust gas conversion for cleaner emissions (Aneggi et al., 2006). They have also been proposed as the reasons why  $\text{CeO}_2$  is effective in increasing combustion rates when mixed with certain other oxides or metals. In a study of the combustion of different hydrocarbons at atmospheric pressure, Zhao et al. (2004) showed that  $\text{CeO}_2$  catalyzed the oxidation of heavier hydrocarbons. Rates increased 1 and 3 orders of magnitude for propane and butane, respectively, but  $\text{CeO}_2$  didn't affect the combustion rates of methane and ethane. Uhm et al. (2004) showed that  $\text{CeO}_2$  enhanced ethanol combustion, increasing volumetric heat release by four times. However, Shi et al. (2003) found increased methane conversion in the presence of Ce, La, and other rare-earth oxides. On a zeolite-supported platinum catalyst prepared by impregnation, methane conversion increased the most with a  $\text{CeO}_2$  additive, and the temperature for 100% conversion was reduced by 50 K.  $\text{CeO}_2$  was also shown to reduce coke formation and initiate a more complete combustion of methane when introduced into a Pt catalyst supported on  $\text{Al}_2\text{O}_3$  (Damyanova et al., 2003). VenDevener et al. (2006) also successfully reduced the onset temperature of oxidation and increased the combustion of JP-10 fuel by 20% in the presence of  $\text{CeO}_2$  nanoparticles. Complete combustion occurred at 1115 K and 1200 K with and without  $\text{CeO}_2$ , respectively. They studied differences between  $\text{CeO}_2$  and  $\text{Fe}_2\text{O}_3$  and found that cerium oxide combusted the fuel to mostly  $\text{CO}_2$  and  $\text{H}_2\text{O}$ , while the iron oxide had no effect. Mixing different alkali metals such as K, Cs, Na, and Rb with  $\text{CeO}_2$  improved its effectiveness in catalyzing diesel oxidation. In the presence of 10% K, the oxidation temperature was lowered by 40 K. The activity of the catalyst was shown to be

dependent on the nature of the alkali metal and its loading (Aneggi et al., 2008). Liotta et al. (2002) showed an increased production of  $\text{CO}_2$  in hydrocarbon combustion with varying amounts of barium added to a  $\text{CeO}_2$  catalyst.

These studies have all shown the ability of rare-earth oxides such as  $\text{CeO}_2$  to enhance overall combustion of different types of fuels. Another positive is that rare-earth oxides can be synthesized in different size ranges fairly easily, unlike boron and other metals in their elemental states. These syntheses will be dealt with in the next section.

#### **1.4 Mixed Metal and Metal/Oxide Syntheses**

Nanoparticle mixtures of boron and metals/oxides like Ti, Al, Fe, or rare-earth oxides could enhance boron combustion by either providing heat release at lower combustion temperatures, or by conducting oxygen ions to the surface of the boron. In preparing such mixtures, the main goals are to obtain a small enough particle size, maintain high surface area, and keep the boron and the other metal (if present) from oxidizing prior to combustion. Starting with elemental boron in the nanoparticles is critical to attaining high energy density.

Boron nanoparticles themselves can be synthesized in many ways. The pyrolysis of decaborane at temperatures between 700-2000 K has been shown to produce boron nanoparticles, but their size distribution is broad and agglomeration is a problem (Casey et al., 1987; Zi et al., 2003). Bellot et al. (2009) synthesized boron nanoparticles by decaborane pyrolysis with a size range of 10-150 nm by passing the gas at 1 atm through a hot zone at 973-1173 K. The ball milling techniques of Van Devener et al. (2009) produced a narrow size distribution of nanoparticles, 40-60 nm. Xu et al. (2004) showed that boron nanoribbons made of micron-sized scroll like structures with 17-20 nm wall thicknesses and 20-100 nm widths

could be made by the same decaborane pyrolysis at lower temperatures. The reduction of boron tri-halides has also been used to make boron nanoparticles (Pickering et al., 2007).

Boron nanoparticles are commercially produced and can be purchased in different size ranges which presumably correspond to passage through mesh sieves. These boron nanoparticles are manufactured by the reduction of  $B_2O_3$  with magnesium. These nanoparticles are not protected from the atmosphere and so acquire an oxide surface layer that can slow combustion (Yetter et al., 1991).

Protecting the boron outer layer from oxidation during synthesis, workup, and transport is therefore of interest. Bellot et al. (2009) functionalized the boron surface with halogens by solution treatment with halogens dissolved in hexane. They showed that the resulting surface was covered by halogen, and no detectable amount of  $B_2O_3$  was present by XPS. The onset temperature of oxidation was determined by DSC experiments. Onset oxidation temperatures were shown to be 803 K for boron, 817 K with fluorine, and 879 K with bromine. Pickering et al. (2007) put an organic cap or barrier on boron nanoparticles in a number of different ways. Van Denever et al. (2009) ball-milled boron nanoparticles in oleic acid and effectively protected the bare boron surface from oxidation upon exposure to air. This was determined by XPS, which showed a significant decrease in surface oxygen for samples milled in oleic acid versus dry milling. Without an oxide layer, the ignition times of boron could be significantly reduced and the overall energy release increased.

Another way to reduce ignition times and to enhance heat release characteristics for boron nanoparticles might be to mix boron with other elemental metals that burn at lower temperatures. The second metals would release the heat needed to increase the local temperature

of the particles and thereby enhance boron combustion. Al, Fe, Ti and others burn at temperatures lower than boron, and composites of these have been prepared by different methods including mechanical milling and wet chemical reductions, for example using  $\text{NaBH}_4$  or  $\text{KBH}_4$ .

Oliker et al. (2008) synthesized Ti-Al-B alloys by ball milling, and found that at longer milling times, the number of TiAl and  $\text{TiB}_2$  composites increased slightly but compositions were dominated by various aluminum and titanium oxides. Tests were not run to determine the oxidation state of the boron in such composites. The introduction of boron in the milling process promoted the formation of a fine crystalline structure, and its homogeneity in the alloy depended on the particle sizes and homogeneity of the original mixture. Mota et al. (2004) used powder technology, a mixture of compaction, sintering, and milling to prepare mixed Al-B composites that were of high boron content. Diffraction patterns suggest that the boron was elemental and the oxides consisted mainly of aluminum. Variations in these processes allowed control over the native oxide layer formation. They studied the differences in milling versus a molten metal compaction technique and found the latter to be more desirable for higher boron content. Kirillova et al. (2000) reduced  $\text{Al}_2\text{O}_3$  at high temperatures (1200-1400 K) with boron to form  $\text{AlB}_{12}$  structures.

Arrested reactive milling is a process proposed to make composites by ball milling boron with metals and certain metal-oxides that are reduced in situ. The idea is that exothermic oxidation of the metal particles by the metal-oxides can be started mechanically, and then continued as driven by exothermic heat release. In many cases, this is done with aluminum as the reducing agent because of its ability to generate substantial heat to increase the local temperature. The key to producing elemental boron particles is to know when to “arrest” the milling and prevent the oxidation reactions of the boron or other second metal (Driezen, 2009).

Schoenitz et al. (2005) showed for arrested reactive milling of Al-Fe<sub>2</sub>O<sub>3</sub> and Al-MnO<sub>3</sub> composites that an optimal time could be determined to “arrest” the reaction just before the spontaneous reaction of oxidation occurred. They formed metal composites that were stable nano-structures at ambient conditions, but ready to react at higher temperature. Mohammad et al. (2009) showed that AlB<sub>12</sub> composites <100 nm in size could be formed after long milling times of Al and B<sub>2</sub>O<sub>3</sub> in a planetary ball mill. By sampling at various time intervals and analyzing the samples by XRD, they determined that no B<sub>2</sub>O<sub>3</sub> or Al remained after 30 h, and after 40 h only Al<sub>2</sub>O<sub>3</sub> and AlB<sub>12</sub> were present. A variation of compaction with a high temperature self propagating synthesis was used by Fu et al. (2010) as a way to make Fe<sub>2</sub>B from Fe<sub>2</sub>O<sub>3</sub>, using Al as the reducing agent. This is similar to arrested reactive milling, in that once initiated, the heat release from Al oxidation is sufficient to keep the reaction going.

Some wet syntheses involving metal reduction have also been reported as ways to make metal-boron composites. FeB was synthesized using anodic templates with KBH<sub>4</sub> and FeSO<sub>4</sub> by Yan et al. (2008), giving ~25% B and 35 nm particles. Reductive processes with KBH<sub>4</sub> and FeSO<sub>4</sub> were also shown by Shen et al. (2004) to produce FeB<sub>2</sub> composites. The final particles were on the same size scale as the initially precipitated material. Resendre et al. (2007) synthesized FeB composites with approximately 13 mol% B by reduction of Fe<sub>2</sub>O<sub>3</sub> with NaBH<sub>4</sub> and HCl. In these cases, the product composites showed little resistance to oxidation in ambient air. To remedy this, Huang et al. (1994) reduced FeCl<sub>3</sub> with KBH<sub>4</sub> in methyl methacrylate (MMA), and found the resulting FeB particles to be less oxidized because there was a 6-7nm MMA covering. They also showed that reduction with mixtures of KBH<sub>4</sub>/ethanol produced smaller particles and size distributions, 30-120nm for KBH<sub>4</sub> and 40-80nm for 10% KBH<sub>4</sub>.

A problem with mixed metal composites is identical to that of pure boron, in that a native oxide layer tends to form on the surface. Mixing boron with certain “non-energetic” fuel additives that could conduct oxygen is a way around this problem. These oxides could provide oxygen directly to the boron-oxide interface and replenish oxygen by adsorption from the gas phase. Bonnetot et al. (2008) prepared  $\text{CeO}_2$  composites with  $\text{B}_2\text{O}_3$  by a sol-gel technique, obtaining low surface areas but good homogeneity. These same oxides were also prepared by co-precipitation and showed good homogeneity (Yuzhakova et al., 2007).

Rare earth composites with a high elemental boron content are of more interest to this project. Tobo et al. (2003) prepared energetic mixtures of rare-earths and boron as  $\text{Ce}_x\text{La}_{1-x}\text{B}_2\text{C}_2$  composites by an argon arc technique. Rare earth diborides of composition  $(\text{RE})\text{B}_2$  were prepared by hot mixing and pressing techniques by Matovnikov et al. (2009). The boride  $\text{LaB}_6$  with a particle diameter of 30 nm was successfully produced by  $\text{B}_2\text{O}_3$  reduction with magnesium at relatively low temperatures (673 K), and particle size was shown to be dependent on the source of boron (Zhang et al., 2008). The borides  $(\text{RE})\text{B}_6$  (RE = rare earth metal) were also prepared by both high temperature mixing (Takeda et al., 2008) and electrochemical synthesis (Bukatova et al., 2007). Through the borothermal reduction of rare earth oxides in a vacuum at 2173 K, Mori et al. (2001) prepared  $\text{ReB}_{25}$  with Gd, Tb, Dy, Ho, and Er.

Therefore, many techniques are known to produce various composites with rare earth metals (or their oxides) and boron. To generate the metallic rare earths, very expensive syntheses at extreme conditions are required. This work is focused on the potential of rare earth oxide (shell)/boron (core) composites for combustion enhancement. No known wet chemical syntheses have been shown to successfully prepare such composites, but a few coating and milling techniques have been studied with varying degrees of success.

The preparation of the reverse system - nano-sized  $\text{CeO}_2$  particles with a BN coating - was demonstrated by Masui et al. (2003). They coated the  $\text{CeO}_2$  nanoparticles with a solution of boric acid and diethanolamine, obtaining an outer covering a few nm thick, which consisted of a mixture of B, BN,  $\text{B}_2\text{O}_3$ , and oxynitrides. Van Devener et al. (2009) prepared B- $\text{CeO}_2$  particles by ball milling and successfully obtained particles in the nano-scale region. They claimed that the boron and cerium oxide particles are chemically bonded and at the interface various  $\text{B}_x\text{Ce}_y\text{O}_z$  compounds existed. They also milled B and  $\text{CeO}_2$  with oleic acid, and found by XPS that the boron was elemental.

### **1.5 Mixed Metal and Metal/Oxide Combustion Studies**

Very few papers have been published on the combustion characteristics of mixed metals and/or metal/rare earth oxide composites. Metals such as Al, Fe, and Ti oxidize much easier than boron, and mixing these with boron may be able to release heat and increase local temperatures, aiding boron combustion (Boichuk et al., 2002). Mg-coated boron particles gave shorter ignition times than boron alone, and the Mg coating helped to remove the boron oxide coating, increasing the amount of boron combusted (Yeh et al., 2006). Rosenband et al. (1995) showed that a Ti coating on boron particles could also reduce ignition times, but this was only true for approximately 8wt% Ti; below this amount the particles did not ignite and above it ignition times were delayed. Sullivan et al. (2009) showed that the addition of nanoscale boron to AlCu mixtures could enhance the overall heat release, and that the local temperature rise from Al combustion significantly enhanced the combustion of boron; they also observed that micron-sized boron was not as effective. Trunov et al. (2008) showed that in methane combustion the addition of Ti to boron powders lowered the conversion temperatures by about 200 K, and they



observed rates (measured by pressure change) were higher for Ti/B composites than for Ti, B, or Al alone.

Mixtures of boron and rare earth oxides have not been extensively studied, and there are no known studies on the effects of adding rare earth oxides to boron particles in hydrocarbon combustion systems.

## CHAPTER 2

### EXPERIMENTAL PROCEDURES

#### 2.1 Particle Preparation

The nomenclature for the particles used in this section will be used throughout. Three grades of boron nanoparticles made by plasma synthesis with Mg as reducing agent were purchased from SB Corporation. According to the vendor, SB99 is 97-99 wt% boron with a nominal size of 60-70 nm, SB95 is 95 wt% boron with a nominal size of 600-700 nm (this sample was characterized by exhaust gas analysis only), while SB86 is 86 wt% pure boron with a particle size of 1-1.2 microns. Starting with SB86, we prepared a ball milled particle sample (“BM”) by milling in a glove box ( $N_2$  environment) for 5 h using 440 Nitronic stainless steel balls at a ball mass/particle mass ratio of 5. Variations on this method (time, ball mass/particle ratio) in trial runs were employed before deciding upon the final procedure. The goal here was to reduce both nanoparticle size and particle agglomeration, while avoiding oxidation of the boron.

Sintered particles (sample name “Sintered”) were made by heating SB86 in a tube furnace for 15 h in 250 mL/min  $N_2$  at 1173 K. Here also, test runs were made to determine the temperature and time that gave the largest (most sintered) particles in a reasonable time, and without excessive boron oxidation.

Boron/rare earth oxide composites were also prepared by ball milling. The rare earth oxide mixture (denoted REOm-41) contained  $CeO_2$ ,  $La_2O_3$ , and  $Gd_2O_3$  with molar ratios Ce/La of 3 and Ce/Gd of 80, prepared by a templated sol-gel procedure developed elsewhere (Kalakota,

2008). In this procedure, measured amounts of precursors cerium (IV) ammonium nitrate (Alfa Aesar 98+%), lanthanum nitrate hexahydrate (Alfa Aesar 99.9%), and gadolinium (III) chloride hexahydrate (Alfa Aesar 99.9%) were dissolved in measured amounts of water and tetra-propyl ammonium hydroxide (TPAOH). The solution pH was brought to 10.4 with aqueous ammonia, and then reacted at 343 K for four days, with the pH periodically returned to 10.4 by ammonia addition. The precipitates were filtered under vacuum, and then washed with DI water, acetone, and DI water. The products were dried at 373 K and calcined in flowing air at 873 K for 5 h. Two blends of the rare earth mixed oxide with SB86 were prepared using the same ball milling procedure mentioned above. Sample BR41-1 consisted of 95 wt% SB86 and 5 wt% REOm-41, and BR41-2 consisted of 80% SB86 and 20% REOm-41.

## **2.2 Particle Characterization**

Particle sizes were determined from a combination of X-ray diffraction (XRD), scanning electron microscopy (SEM) and porosimetry. XRD was used to determine the crystalline phases of boron and boron oxides, while thermo-gravimetric analysis (TGA) in air was used to measure “active” (meaning elemental boron) content. Characterization was performed on both feed and burnt particles collected from the exhaust plenum of the combustor.

XRDs were taken at both the College of Engineering’s MCC (Materials Characterization Center) and at LSU CAMD (Center for Advanced Microstructures and Devices). At MCC, the diffractograms were collected on a Rigaku Mini-Flex diffractometer using Cu K $\alpha$  radiation. All samples were analyzed at  $2\theta$  values from 5 to 75°, with a step size of 0.02°, and a rate of 1°/min. At CAMD, data was collected on a Huber four-circle diffractometer with a Canberra detector capable of radiation in the range of 4-10 keV (Cr K $\alpha$ -Zn K $\alpha$ ). Radiation close to 8.04 keV (Cu

K $\alpha$ ) was obtained by tuning the double crystal monochromator to an approximate value so that 2 $\theta$  corrections were not necessary. Samples were analyzed at 2 $\theta$  values from 5-75° with a step size of 0.02° at 0.1°/min. In both cases, data analysis was performed using MDI's Jade software with background removal. Particle size estimates were calculated using the Scherrer equation:

$$\text{crystal size (nm)} = \frac{K*\lambda}{FWHM*\cos(\theta)} \quad (2.1)$$

where K is the shape factor, assuming the typical value of 0.9,  $\lambda$  is the wavelength of the source, at MCC 1.54 nm and CAMD 1.52 nm (wavelength was obtained by refining with a NIST LaB<sub>6</sub> standard), and FWHM is the full width of the peak at half height. Diffractograms were compared to those from the International Center for Diffraction Data's (ICDD) database in order to identify the crystalline phases of boron.

SEM imaging was done on an FEI Corp. Quanta 3D SEM at 5kV and 20,000-80,000 magnification. To reduce the effects of charging, the particles were coated with gold by sputtering.

Porosimetry was done using a Quantachrome AS-1 porosimeter by N<sub>2</sub> adsorption-desorption. Surface areas were calculated from the adsorption branch by the BET method, using points below P/P<sub>sat</sub> = 0.3. Pore volume distributions were calculated using the desorption branch by the BJH method. Average particle diameters were calculated by the following:

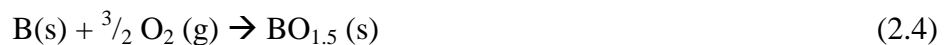
$$\text{average particle diameter} = \frac{6}{\rho*S.A.} \quad (2.2)$$

where  $\rho$  is boron density (2350 kg/m<sup>3</sup>) and S.A. the surface area measured in the experiment. Particle diameters were calculated assuming perfectly spherical and non-porous solid particles. Average pore diameters were calculated using the BJH distribution as follows:

$$\text{average pore diameter} = \frac{\int_0^{\infty} \frac{dV}{dD} * D * dD}{\int_0^{\infty} \frac{dV}{dD} * d(D)} \quad (2.3)$$

where  $d(V)/d(D)$  was computed in machine software by the BJH method,  $V$  is pore volume, and  $D$  is pore diameter.

The “active” (meaning elemental boron) particle content was determined by weight change using a Perkin-Elmer TGA 7. The samples were first dried in 50 mL/min He starting at 323 K, with a 10 K/min ramp to 673 K and a final hold of 20 min. At this point, the gas was changed to 50 mL/min of air, and then ramped at 5 K/min to 1073 K, with a 12 h final hold. The active boron content was determined from the weight increase upon oxidation. The stoichiometry for boron oxidation was assumed to be:



Active boron content is:

$$\text{active boron (mol\%)} = \frac{\text{moles B}}{\text{moles B} + \text{moles BO}_{1.5}} * 100 \quad (2.5)$$

The challenge was determining the amount of B<sub>2</sub>O<sub>3</sub> in the initial sample. To do so, the following mass balance equation was used:

$$Z = (\omega * \text{wt}_{\min}) - ((\text{wt\%}_{\text{gain}}/100) * \text{wt}_{\text{initial}} * \frac{MW_B}{MW_{\text{BO}_{1.5}} - MW_B}) \quad (2.6)$$

where  $z$  is the dry weight of  $B_2O_3$ ,  $\omega$  is the dry weight fraction of the sum of B and  $B_2O_3$  initially,  $wt_{min}$  is the minimum weight of the sample after the loss of water,  $wt\%_{gain}$  is the change in wt% from  $wt_{min}$  to the maximum weight, and  $wt_{initial}$  is the initial sample weight. The calculated “Z” was used to determine the mol% of active boron by the following equation:

$$\text{active boron (mol\%)} = \frac{\frac{wt_{initial} * wt\%_{gain} / 100}{MW_{BO1.5} - MW_B}}{\frac{wt_{initial} * wt\%_{gain}}{MW_{BO1.5} - MW_B} + \frac{z}{MW_{BO1.5}}} \quad (2.7)$$

### 2.3 Combustion Setup and Particle Collection

Combustion experiments were performed with the Acharya group in LSU Mechanical Engineering. The combustion apparatus is shown in Figure 2.1. In all cases an equivalence ratio ( $\phi$ ) of 0.69 was used and is defined as the ratio of the actual to stoichiometric fuel/air ratios:

$$\phi = \frac{\frac{fuel}{air}_{actual}}{\frac{fuel}{air}_{stoichiometric}} \quad (2.8)$$

Air was introduced through primary (inner) and secondary (annular) inlets. Ethanol was supplied from a pressurized tank and injected through 0.3 mm orifice atomizers. Boron nanoparticles were injected into the system using a reverse cyclone system as shown in Figure 2.2. Flow characteristics of the air, fuel, and nanoparticles were studied to optimize the delivery system (Karmakar et al., 2010), but are not within the scope of this thesis. Fitted holes along the side of the combustor section in Fig. 2.1 allowed for both burnt particle collection and temperature measurement. Temperature was measured by a thermocouple assembly inserted into one of these holes; the assembly contained five thermocouples at different radial locations. A 3/8” line fitted to the hole nearest the exit of the combustor was used to collect burnt particle

samples. An in-line filter was inserted above the ball valve (Fig. 2.1), while a vacuum pump was used for suction. A typical run lasted 1 min, and one gas sample was collected per run.

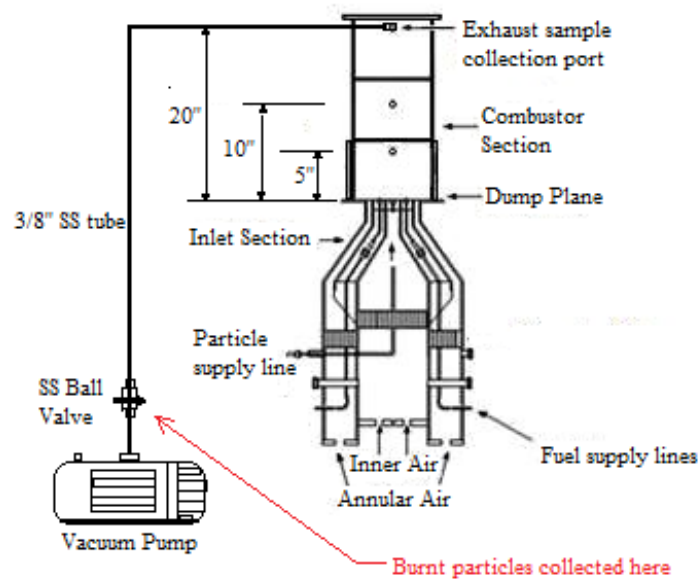


**Figure 2.1: Combustion apparatus (Karmakar, 2011)**

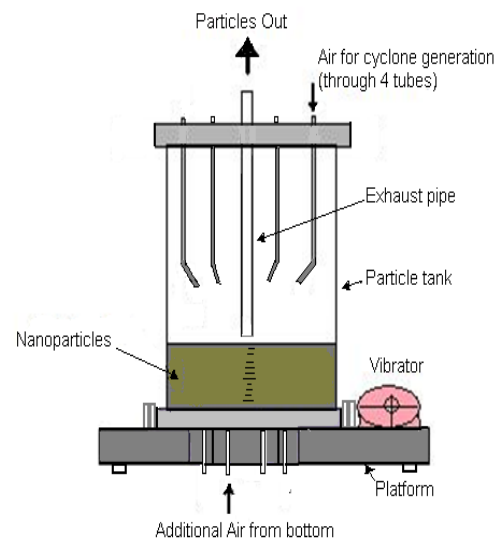


**Figure 2.2: Particle injection system (Karmakar, 2011)**

## 2.4 Exhaust Gas Analysis

Exhaust gas samples were collected in the same way as the burnt particles, except a 316 stainless steel sample cylinder was placed in line with the vacuum pump. Samples were obtained and analyzed during the course of several changes to the combustion unit; these changes are documented here and as discussed in Chapter 3 they probably changed the unit's performance. Case 1 denotes the original setup where the tubing connecting the exhaust plenum and the vacuum pump contained various unnecessary fittings. In Case 2 (shown in Fig. 2.1), this setup was replaced by a single line. In Case 3, the particle injection method was switched from injection of particles with the primary air flow to the particles being injected independently at the centerline. These samples were analyzed on a Varian CP-3800 gas chromatograph fitted with a thermal conductivity detector (TCD). An Alltech CTR 1 dual packed column with a 1/4" outer column packed with activated molecular sieve and a 1/8" inner column packed with a porous polymer mixture was used for separation. Helium was the carrier gas and all compositions were calculated on a dry basis. Retention times were determined by injected known standards into the column and measuring their elution times. The split ratio between columns was determined by injecting various air/CO<sub>2</sub> standards and taking the area ratio of air(inner) to the sum of air(inner), O<sub>2</sub>(outer), and N<sub>2</sub>(outer). The split ratio was consistently calculated at 0.39. Raw areas were converted to mol% by first calculating a modified area that accounts for the total area from each species by using the split ratio. For CO<sub>2</sub>, using the raw area of the inner column:

$$\text{modified area} = \text{raw area}/0.39 \quad (2.9)$$

For O<sub>2</sub> and N<sub>2</sub> using the raw area of the outer column:



$$\text{modified area} = \text{raw area}/(1-0.39) \quad (2.10)$$

The modified areas account for the total amount of species in both columns, and were converted to raw mol% by:

$$\text{raw mol\%} = \text{modified area}/\text{total modified area} \quad (2.11)$$

Raw mol% for each species was then corrected by T.C. response factors given by Dietz (1967) and listed in Table 2.1. T.C. response factors are calibration factors that account for the intensity differences on the signal output of thermal conductivity detectors by different species. Raw mole fractions were corrected by:

$$\text{corrected mol\%} = \text{raw mol\%}/\text{T.C. factor} \quad (2.12)$$

Calculated mole fractions were then determined by dividing the corrected mol% by the total corrected mol%, and is what is reported in Chapter 3. Further details on the chromatography are given in Appendix 1.

**Table 2.1: T.C. Response Factors (Dietz 1967).**

T.C. Response	Compound
1.2	CO <sub>2</sub>
1	O <sub>2</sub>
1.05	N <sub>2</sub>

## CHAPTER 3

### RESULTS AND DISCUSSION

#### 3.1 Initial Particle Size, Structure and Composition

All XRD diffractograms are given in Appendix B. The data corresponding to SB99 and SB86 are given in Figure 3.1, and show major peaks at  $2\theta = 36.8^\circ$  and  $43.0^\circ$ . Both peaks are characteristic of  $\alpha$ -rhombohedral boron (JCPDS PDF# 12-0377). The broad peak widths suggest that the crystalline phase is composed of nanoparticles.

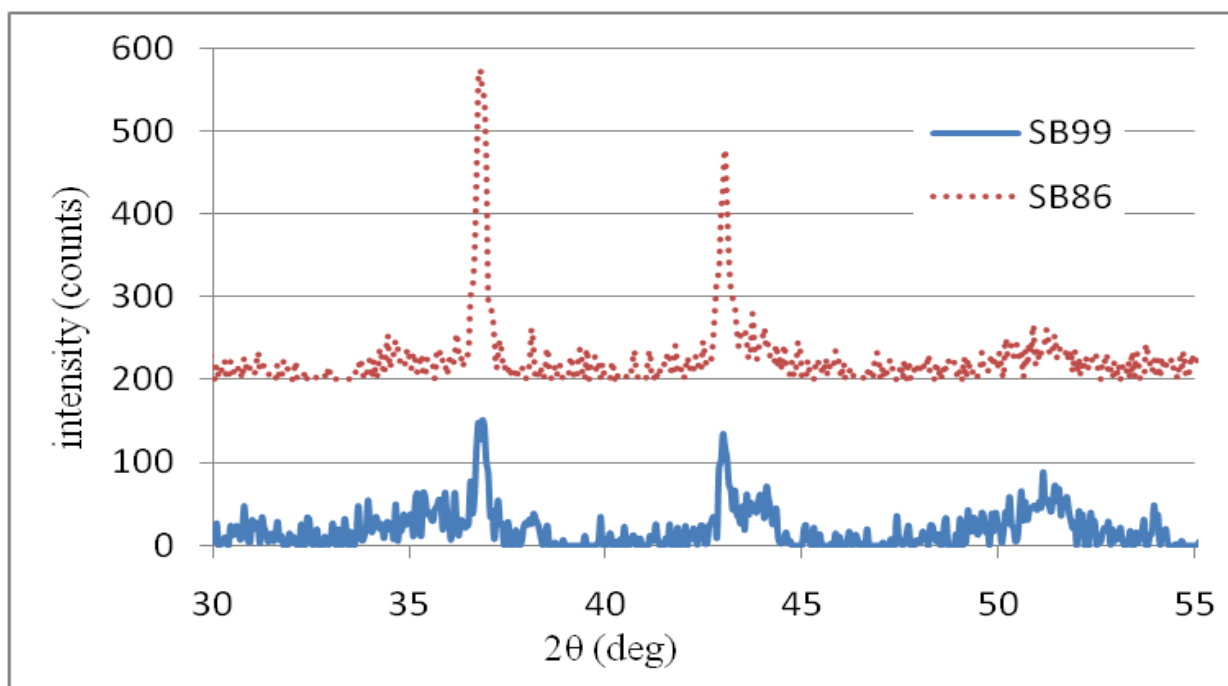


**Figure 3.1: X-Ray diffractograms of SB99 and SB86.**

The “Sintered” sample’s diffractogram (Fig. 3.2) shows a distinct peak at  $2\theta = 27^\circ$ , confirming the presence of crystalline  $B_2O_3$  (JCPDS PDF# 06-0297). In the sintering process, the oxide layer crystallized under high temperature (1173 K), resulting in a detectable amount of crystalline oxide. No detectable amounts of crystalline boron were present in the sintered sample. The BM, BR41-1, and BR41-2 samples (Fig 3.2) show no significant peaks in the region

scanned, and so appear to be composed of amorphous or very small particles. In each case, a small peak at  $2\theta = 36.8^\circ$  confirms the presence of some crystalline boron, but the intensity is weak. The mechanical milling process used in the preparation of these samples may have broken down the larger crystallites present in the starting materials. In the case of BR41-2, there was also a small peak at  $2\theta = 29^\circ$ , indicative of  $\text{CeO}_2$  (JCPDS PDF# 34-0394). The milling process with rare-earth oxides may have oxidized some of the boron, while reducing some  $\text{CeO}_2$ , partly accounting for the weakness of this peak.

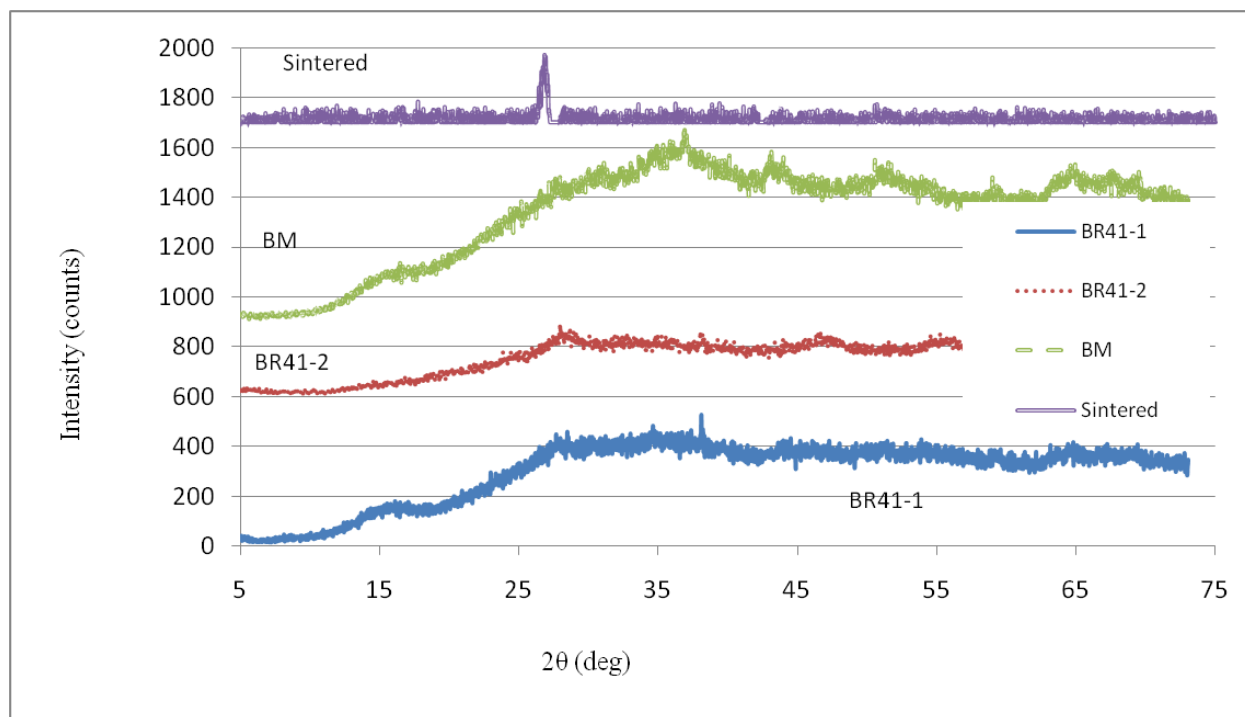


**Figure 3.2: X-Ray Diffractograms of Sintered, BM, BR41-1, and BR41-2.**

The diffractograms collected at CAMD confirmed the other XRD results for SB99 and SB86; however, BR41-1 (Fig.3.3) showed many peaks indicative of rhombohedral boron, (JCPDS PDF# 11-0618 and 12-0377) and a strong peak for crystalline  $\text{B}_2\text{O}_3$  ( $2\theta = 27.6^\circ$ , JCPDS PDF# 30-0019). The absence of any peaks representative of the rare-earth oxides confirms that they are present as nanoparticles, or dissolved in the boron phase.

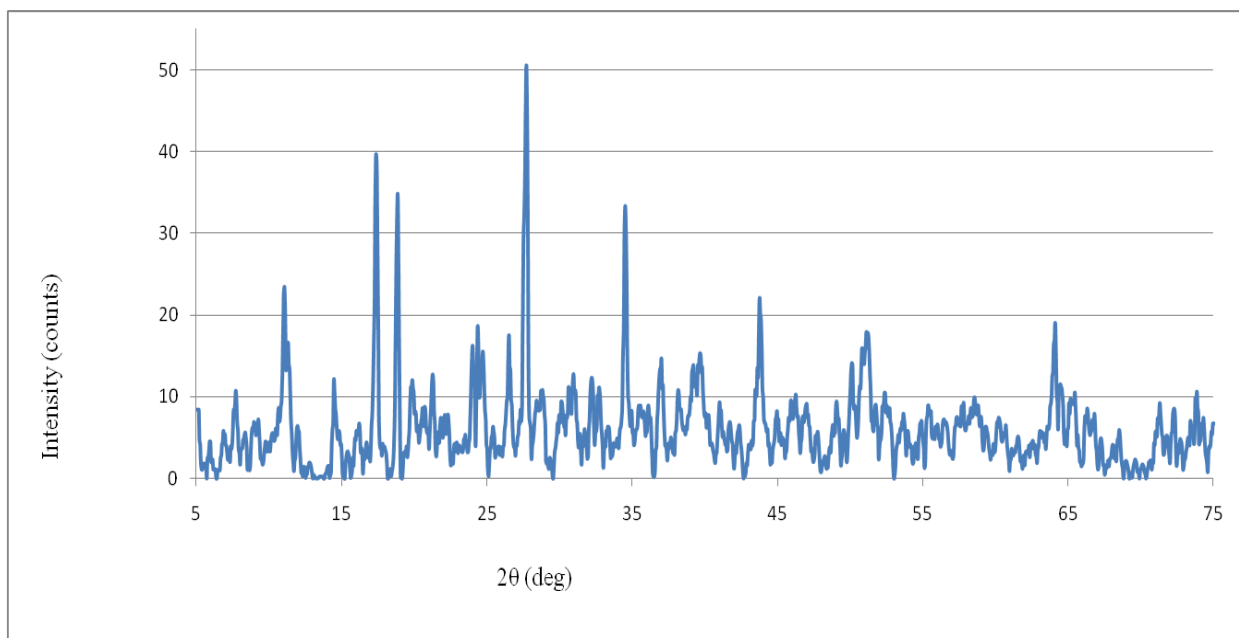


**Figure 3.3: X-Ray Diffractogram of BR41-1 collected at CAMD.**

Particle sizes were calculated by the Scherrer equation for SB99 and SB86 only, because only for these two samples were the peak intensities large enough. Table 3.1 gives the calculated particle sizes calculated from the diffractograms shown in Fig. 3.1; these sizes represent the larger crystallites only, not amorphous particles or very small crystallites. The calculated crystallite sizes are slightly larger for SB86 than SB99. The data show that SB99 and SB86 contain some crystalline boron, both with similar crystal sizes, while BM, “Sintered”, BR41-1, and BR41-2 are mostly amorphous boron.

**Table 3.1: Scherrer calculations for SB99 and SB86.**

Sample	Peak (2θ)	Size (nm)	Peak (2θ)	Size (nm)
SB99	36.9	240	43.0	270
SB86	36.8	280	43.0	340

SEM images were used to study the agglomeration and physical homogeneity of the samples; these images are shown in Figures 3.4-3.6. In the images of SB99 and SB86 (Fig. 3.4),

the primary particle sizes in each appear similar (20-100 nm), although a few particles are larger. Some of the larger particles look to be partly sintered aggregates of more primary (<100 nm) particles, but these images do not give sufficient detail to see any differences between the two. Note that the larger, more rounded or smoother particles are probably more crystalline, and according to Table 3.1 the crystalline particles of SB86 are actually slightly larger than those of SB99. However, both the SEM and XRD data suggest only minor morphological differences between the two samples.

The SEMs of BM, BR41-1, and BR41-2 (Figs. 3.5 and 3.6) also show numerous aggregates of the more primary particles. Some of these aggregates appear larger in these samples than in either SB99 or SB86; this could be due to caking and further agglomeration in the ball mill. These three samples appear similar because they were prepared in the same fashion with the same starting boron material. In the case of the two mixtures containing the mixed rare-earth oxide REOm-41, the SEMs cannot differentiate between boron and REOm-41. The SEM images show no distinct differences between SB99, SB86, BM, BR41-1, and BR41-2.

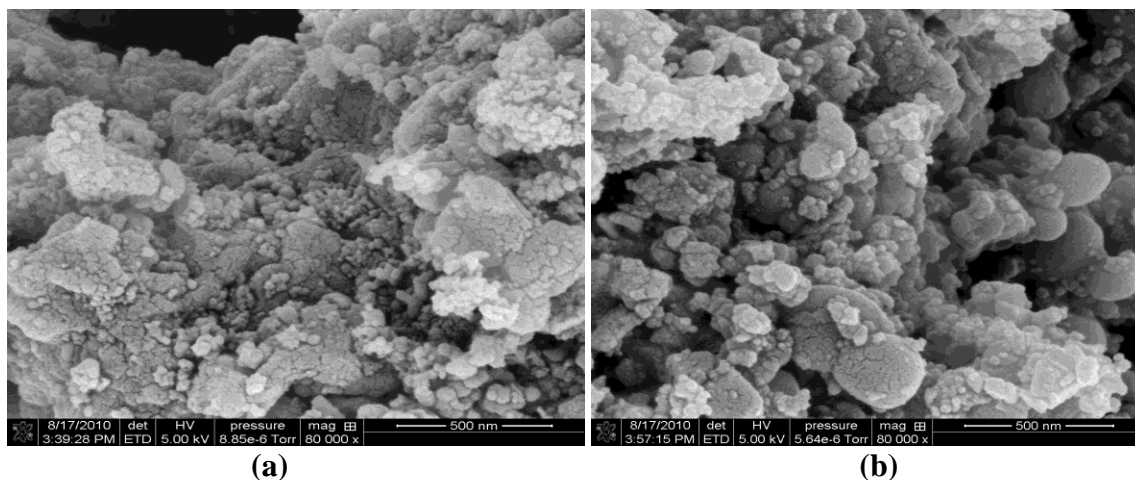


**Figure 3.4: SEM images of SB99(a) and SB86(b). 80,000X magnification, 500nm scale (Karmakar, 2011).**

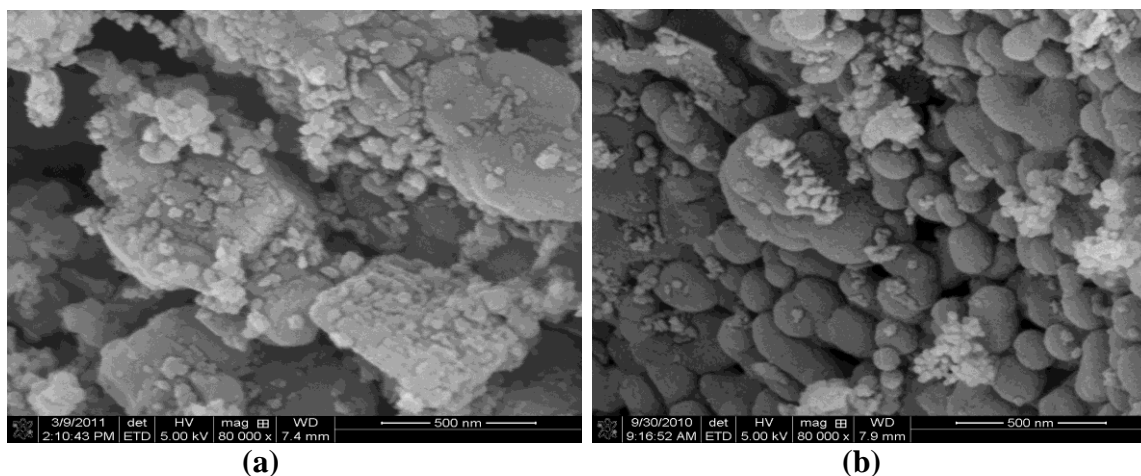


**Figure 3.5: SEM images of BM(a) and "Sintered"(b). 80,000X magnification, 500nm scale (Karmakar, 2011)**

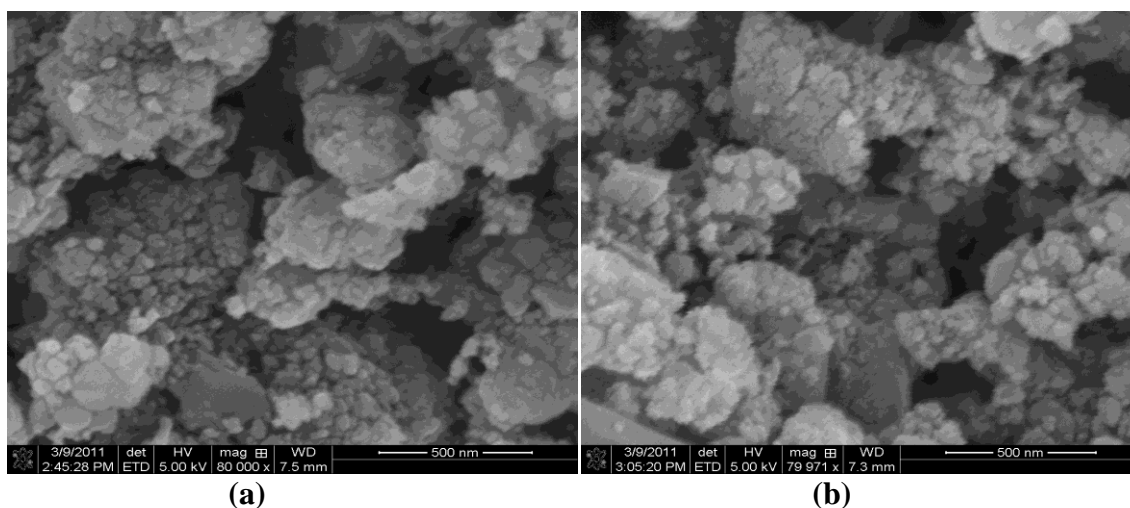


**Figure 3.6: SEM images of BR41-1(a) and BR41-2(b). 80,000X magnification, 500nm scale (Karmakar, 2011).**

The SEM of the "Sintered" sample shows distinct differences from the others. The sintering process contracted the more porous structure of the aggregates, gave the particles more rounded features, and the particles appear to be solid particles in the range of 100-300 nm.

Surface area, pore volume, and pore diameter measurements for the samples are given in Table 3.2. "Primary" particles refer to the smaller particles that make up the larger agglomerates; the surface area gives an estimate of the size of the primary particles, because it is evident from both the SEMs and the pore size distributions that there are some pores or spaces between

primary particles. Assuming that within agglomerates the sintered contact area between particles is negligible, the surface area is essentially a measure of the total areas of the individual primary particles. The assumption of no partial sintering overestimates the size of the primary particles, because there is no surface area for N<sub>2</sub> adsorption in areas where two particles exactly touch.

Particle diameters were calculated using Equation 2.2 assuming the individual primary particles are perfectly spherical, non-porous solid particles; these calculated diameters for SB99, SB86, and BM were the same, ~70 nm. This suggests that ball milling does not affect primary particle size. The decreased surface area in the “Sintered” sample results in larger calculated primary particles (~100 nm), consistent with what was seen in the SEM images. Samples BR41-1 and BR41-2 have higher surface areas due to the presence of the REOm-41, which by itself has a surface area of approximately 120 m<sup>2</sup>/g. Because of this strong influence of the rare-earth oxide on the composite’s surface area, no calculations of boron particle diameters could be made for BR41-1 and BR41-2, but we expect them to be similar to BM because they were prepared in a similar manner.

**Table 3.2: Particle characteristics determined from N<sub>2</sub> adsorption-desorption measurements.**

Sample	SB99	SB86	BM	Sintered	BR41-1	BR41-2	REOm-41
Surface area (m <sup>2</sup> /g)	35	36	38	26	40	53	120
Pore volume (cc/g)	0.16	0.20	0.19	0.15	0.18	0.16	0.15
Avg. pore diameter (nm)	6.1	9.5	37	39	34	27	9.8
Calculated particle diam. from surface area (nm)	72	71	68	100			

Figures 3.7 and 3.8 show cumulative and normalized pore size distributions, respectively. Because less than 10% of the total pore volume is contained in pore diameters less than 5 nm (Fig. 3.7), the total pore volumes (values given in Table 3.2) represent primarily crevices between agglomerates and larger pores within agglomerates. There appear to be few pores inside

primary particles. A larger total pore volume indicates less efficient packing; in the case of SB86 and BM compared to SB99, it indicates larger or more irregularly-shaped agglomerates. A larger pore volume and average pore diameter for SB86 compared to SB99, coupled with the fact that they consist of the same size primary particles, suggests that SB86 is made up of larger agglomerates than SB99. This is also consistent with the vendor's specifications for particle size based on Fisher sub-sieve measurements; these were 1 micron maximum for SB86 and 62 nm for SB99 (SB Boron Corp.). With the primary particles being the same size, the vendor's sieve measurements were based on the size of agglomerates.

The differences between BM and the REOm-41 mixtures arise from the rare-earth oxides which contain meso- and micropores. The pore volume of "Sintered" is slightly less than the other samples, and its average pore diameter larger, because the sintering process contracted the pore space within the agglomerates, as was seen in the SEM images. Fig 3.8 shows that SB99 and SB86 contain some small pores <10 nm, indicative of small pores within the agglomerates or possibly even the primary particles; these pores were eliminated by either ball milling or sintering (see Fig. 3.8). This is seen in the measured average diameters (calculated from Equation 2.3) also; the average diameters are much smaller for SB99 and SB86 than for BM or "Sintered". Both BR41-1 and BR41-2 contain larger numbers of pores <5 nm because of the porous microstructure of the rare-earth oxides. In summary, the data show that SB99, SB86, and BM contain similar-sized primary particles (~70 nm assuming perfect spheres) that make up aggregates of increasing size or more irregular shape from SB99 to BM to SB86, and the data confirm that the "Sintered" particles are indeed larger (~100 nm assuming perfect spheres) with few intraparticle pores.



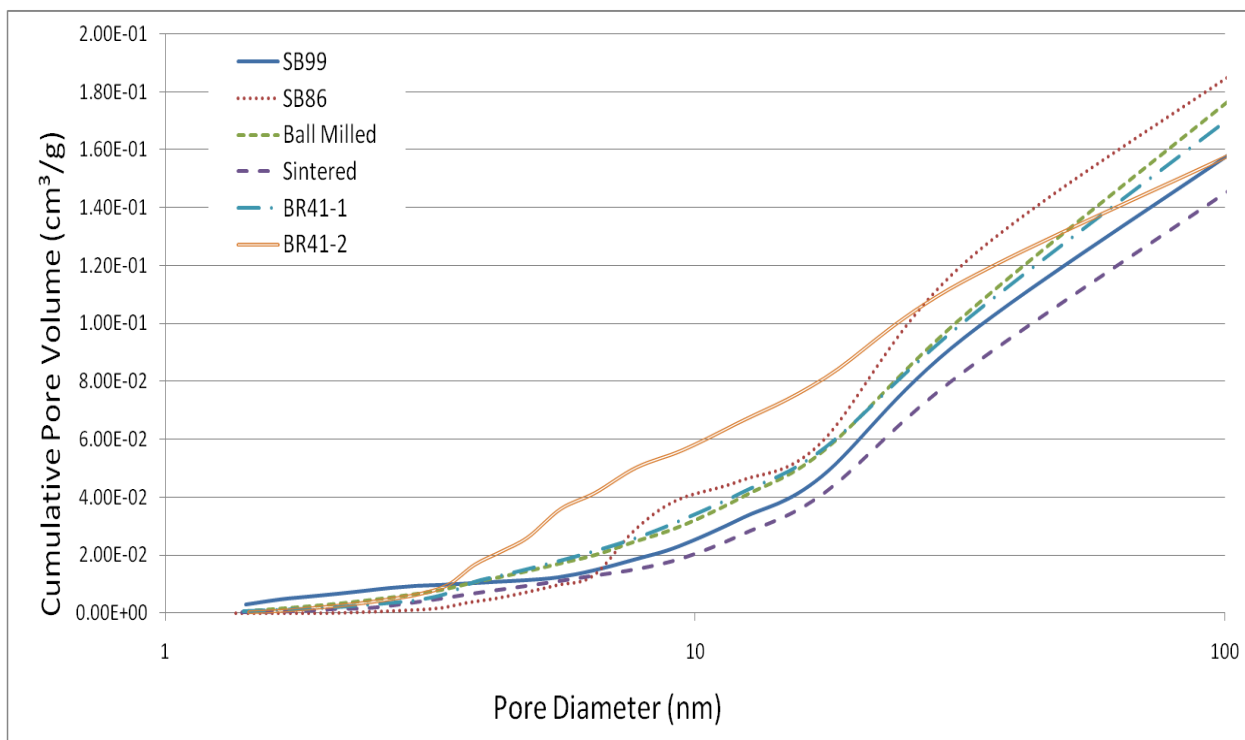


**Figure 3.7: Cumulative pore volume distribution as computed by the BJH desorption method.**

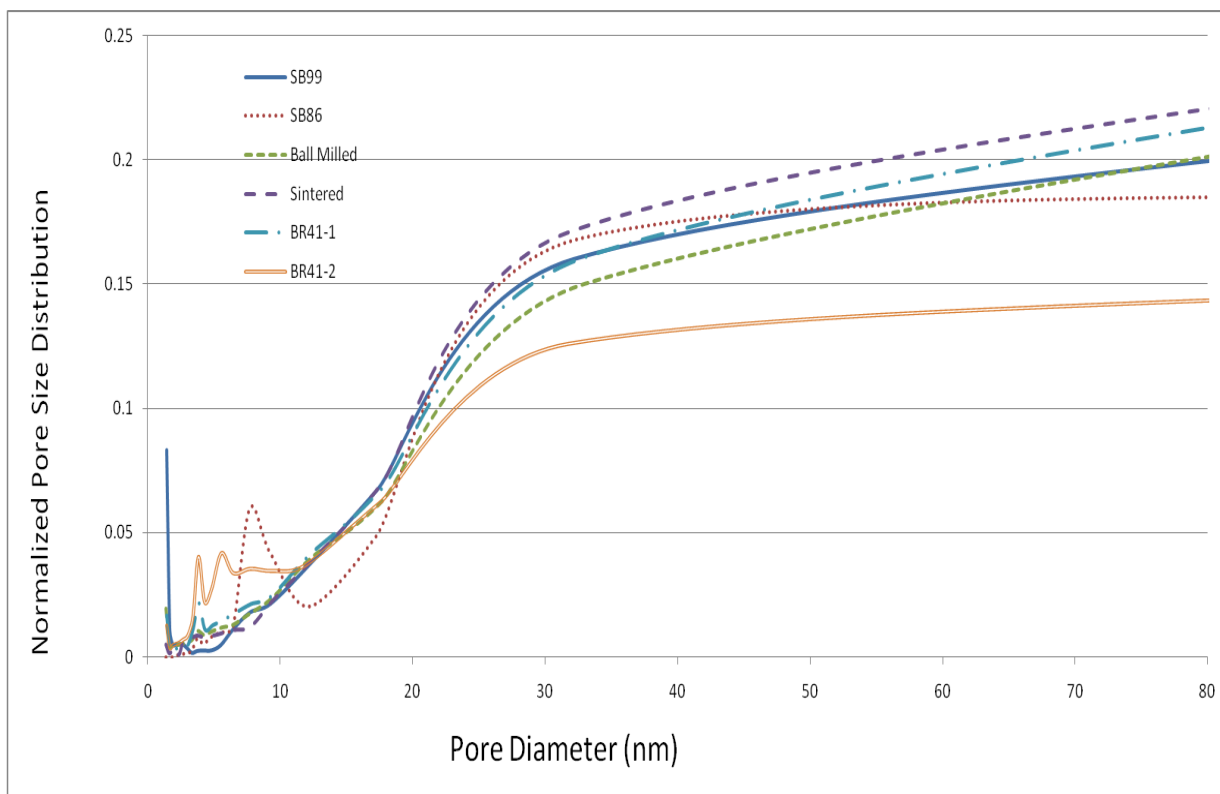


**Figure 3.8: Normalized pore size distribution as a function of pore diameter.**

The calculated measures of “active” particle content are given in Table 3.3. Active content means the fraction of the original boron particles that is composed of elemental boron and is therefore active for oxidation.

**Table 3.3: Active particle contents and maximum oxidation temperatures from TGA measurements in air.**

Sample	SB99	SB86	BM	Sintered	BR41-1	BR41-2
Active content (mol%)	85.1	88.1	75.7	92.1	78.6	79.3
Average oxidation T (K)	1043	1066	1008	1066	1066	1066

The “Sintered” sample has the highest active particle content, due to the high temperature reduction that was used in its preparation. The SB86 and SB99 samples have relatively high active boron contents, only a bit lower than the vendor specifications. This represents some oxidation in shipping and handling. The low percentage active contents for the BM and rare-earth composite samples result from the ball milling method used in their preparation. Ball milling causes agglomerates to break apart, uncovering some bare boron which can be oxidized upon contact with air. Despite the reduction of elementary boron in the ball milled samples, most of the boron content is still elemental boron.

These TGA results are plotted against time in Figs. 3.9 and 3.10. For all data, the temperature – time history is the same; a time of 75 min corresponds to 765 K, 100 min to 887 K, 125 min to 1016 K and 135 min to 1066 K, which was the final hold temperature. The average oxidation temperature of each sample can be an indicator of its ignition temperature in combustion environments. The average oxidation temperature in Table 3.3 was taken as the maximum of the derivative curve in Fig. 3.10. The data (Table 3.3) show that SB99 and (especially) BM are oxidized at lower temperatures than the other samples. The agglomerate size

difference between SB99 and SB86 suggested by the porosimetry data and the vendor's specifications could have an effect on combustion, because in the TGA SB99 oxidizes at lower temperature than SB86. These results also suggest that the BM sample could burn rapidly in a combustor. Notice that in the case of the larger "Sintered" particles, oxidation occurs at a much slower rate and at higher temperatures. The higher oxidation temperatures (compared to SB99) of the mixed rare-earth oxide samples suggest that the presence of these oxides could have a negative effect on boron combustion, contradicting the idea that the rare-earth additives can rapidly conduct oxygen to the boron surface.

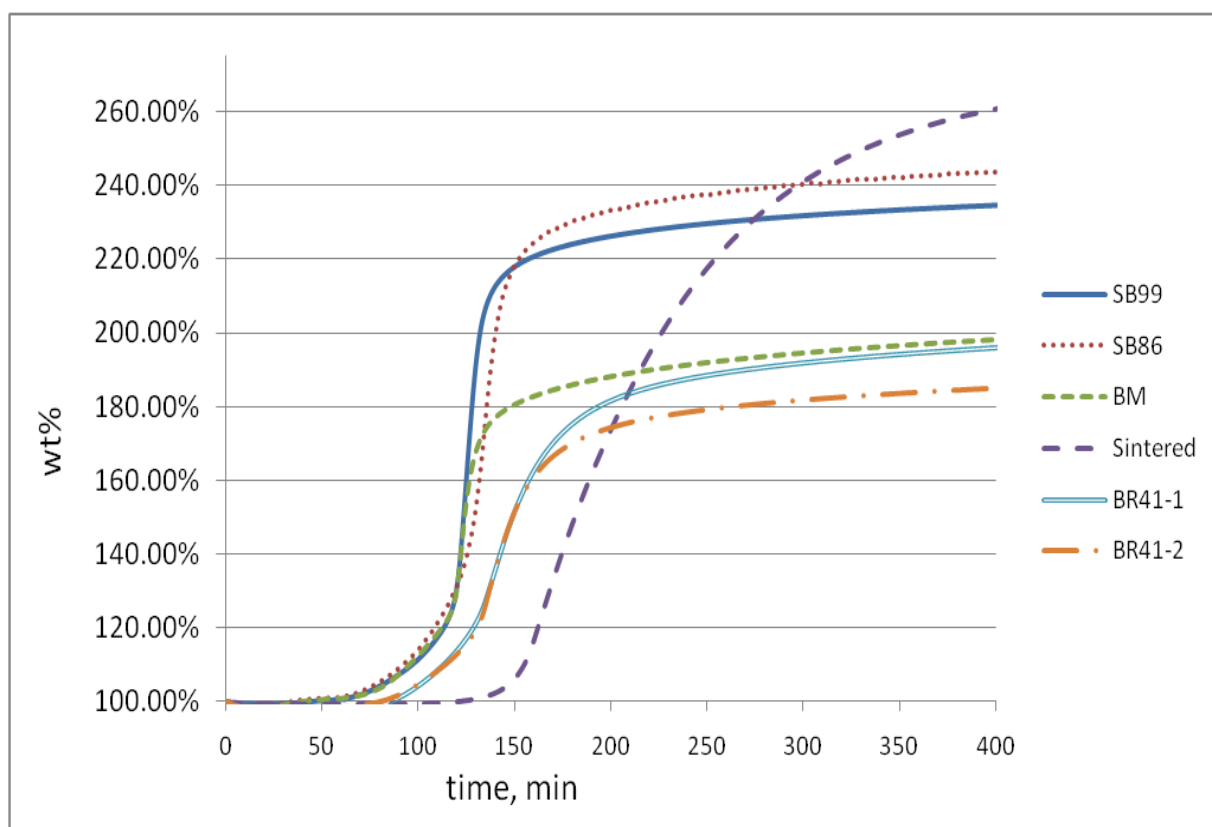


**Figure 3.9: TGA analysis in air for boron and boron/REO nanoparticles.**

Therefore the TGA data show that the average boron oxidation temperature increased with increasing primary particle size, and could also be dependent on agglomerate size. In Figure

3.10, the magnitude and location of the derivative peaks hint at the rates of combustion and the ability to supply oxygen to the bare boron surfaces. However, it should be recalled that TGA experiments differ greatly from conditions in an actual combustor. In a TGA, there is a small bed of particles rather than fluidized particles, so  $O_2$  transport may be slower in the TGA. There may also be no way to remove a molten  $B_2O_3$  layer in the TGA, since the particles are packed tightly together. In TGA, the temperatures are lower than those in the combustor; the maximum temperature in the TGA is restricted to 1270 K. Finally, the gas environment of the combustor differs in several respects from the pure air environment of the TGA. Therefore one should be careful about extrapolating these trends for all types of particles. The main purpose of the TGA experiments was to determine the actual “active” boron content, not to discover the exact ways in which the particles would burn in a commercial combustor.

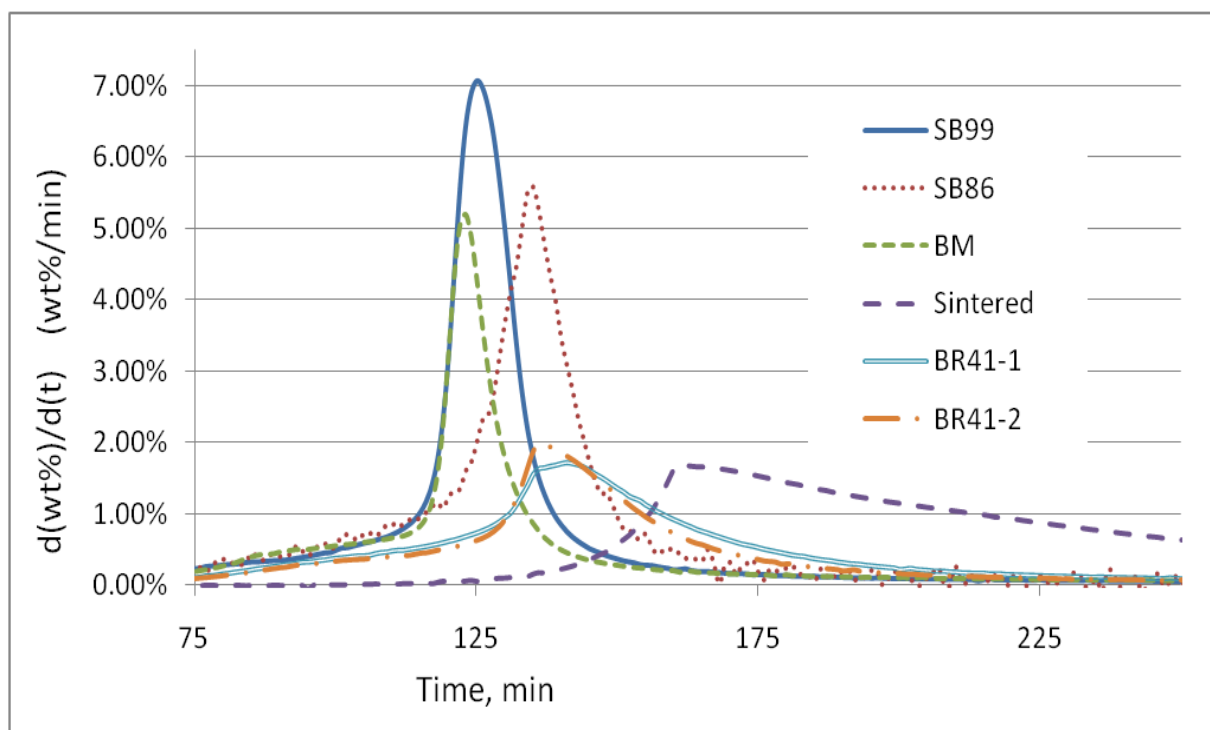


**Figure 3.10: Derivative TGA for boron and boron/REO nanoparticles.**

ICP-AES (inductively coupled plasma atomic emission spectroscopy) was carried out on SB99 and SB86 to determine the amount of magnesium remaining in the samples; some magnesium is inevitable from the magnesium reduction process used in manufacturing. Both samples show small amounts of magnesium (Table 3.4), about 3 wt%; SB99 contains slightly more Mg than SB86. Any elemental magnesium present would add to the overall heat release of the particles, while magnesium oxide would detract from the heat release.

**Table 3.4: ICP results for magnesium content.**

	SB99	SB86
Wt% of Mg	3.4	3.0

### **3.2 Boron Nanoparticles - Performance in Combustor**

Temperature data from the combustor are given in Figures 3.11-3.13. Particle temperatures were measured at different locations above the dump plane, which is the location where air, fuel, and particles are injected into the system (see Fig. 2.1). The exit of the combustor is 20 in above the dump plane, and this is where the temperatures of all samples were measured in Figures 3.11-3.12. In Figure 3.13, temperatures for SB99 and SB86 were also measured 15 in. above the dump plane. The temperatures are plotted against radial distance from the centerline of the combustor. The data show an increase in temperature, at any given radial distance, when boron nanoparticles are used, except in the case of the “Sintered” particles. This proves that the presence of boron particles can increase the overall heat release in ethanol combustion, but the mechanism is complex enough that it is particle (size, morphology)-dependent.

Temperatures measured at the exit show that SB86 had a greater overall effect on temperature than either SB99 or BM, but a closer look at the data collected below the exit shows that SB99 caused more heat release at elevations nearer the dump plane, indicative of faster ignition and burning times for SB99. This shows that the increasing agglomerate size from SB99

to SB86, suggested by the porosimetry data and the vendor's specifications, decreases ignition and burning rates. Below the exit, the temperatures without particles were very similar to those for SB86, again suggesting that the combustion of boron in the more agglomerated SB86 was more delayed. In their work with boron nanoparticles ~60 nm, Young et al. (2009) concluded that ignition and burning rates were strongly dependent on agglomeration of the primary particles, and our results confirm this conclusion, as the more agglomerated particles apparently had a delayed heat release. This can be because in more agglomerated particles there is greater resistance to oxygen diffusion. From the TGA data, we expect BM to act in a similar manner to SB99, burning faster and releasing nearer to the dump plane.

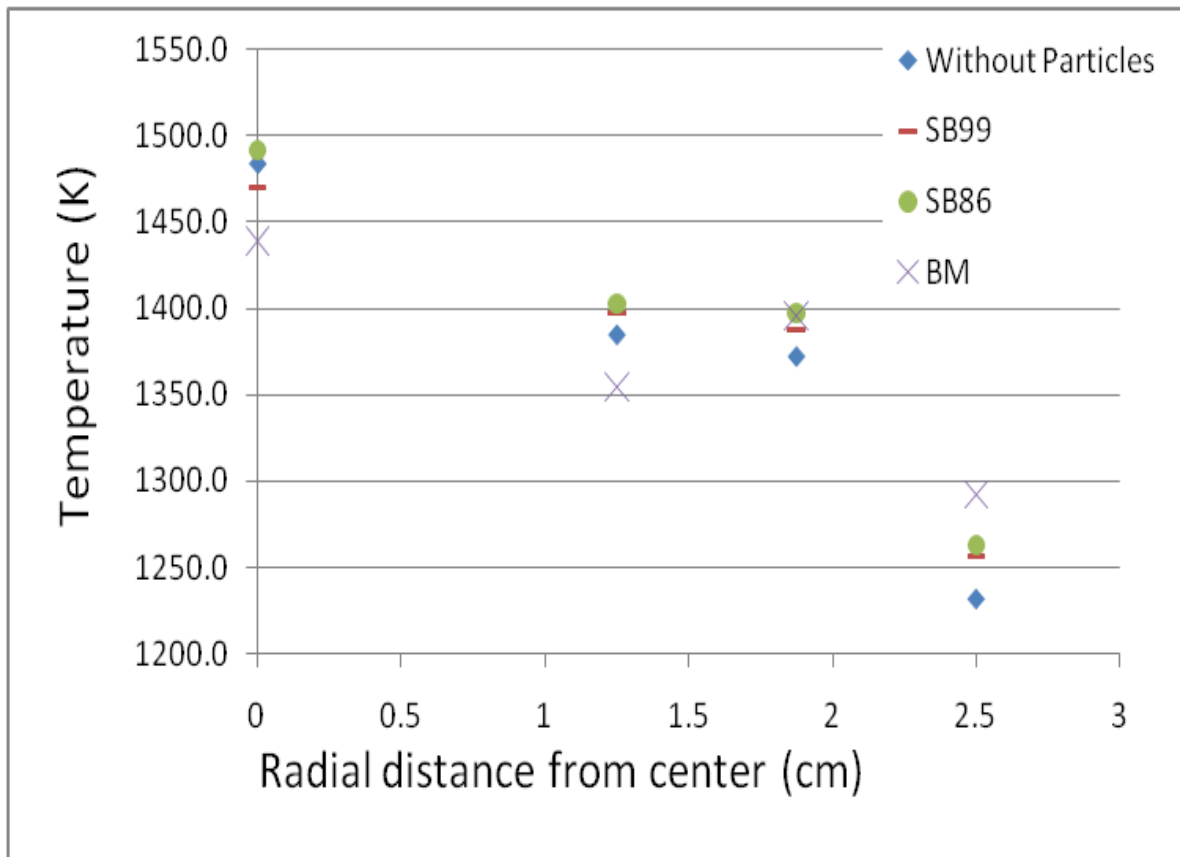


**Figure 3.11: Temperature data for SB99, SB86, and BM at exit (20in. above dump plane) (Karmakar, 2011).**

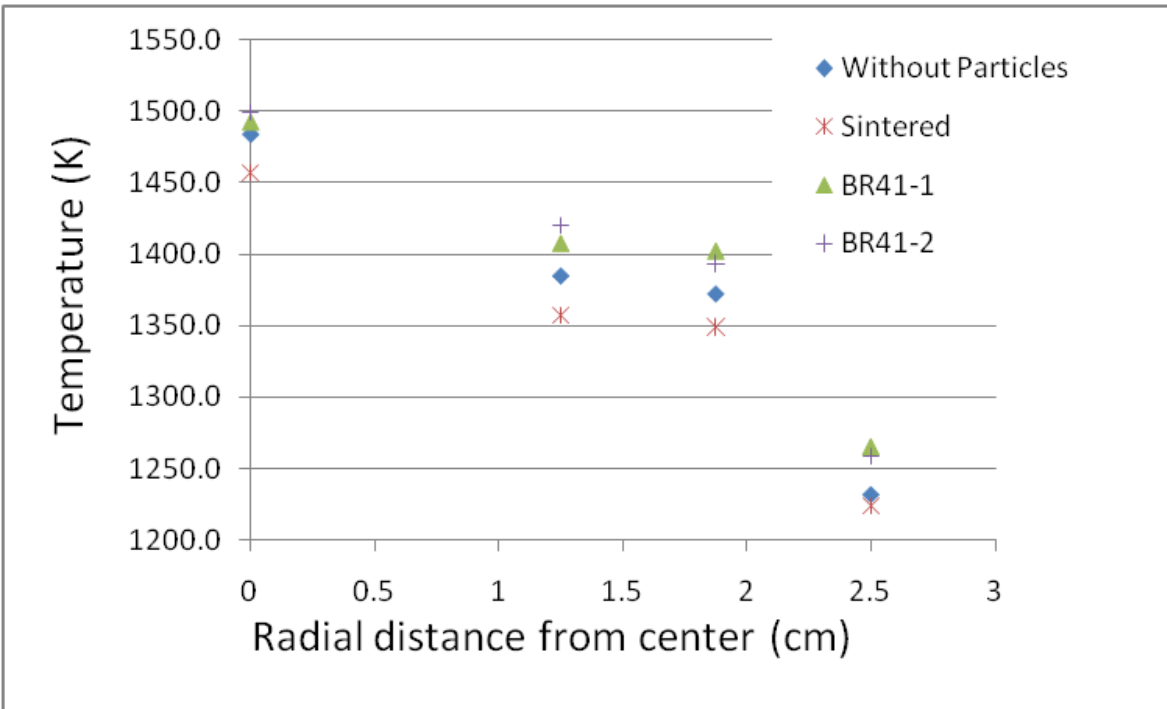


**Figure 3.12: Temperature data for Sintered, BR41-1, and BR41-2 at exit (20in. above dump plane) (Karmakar, 2011).**

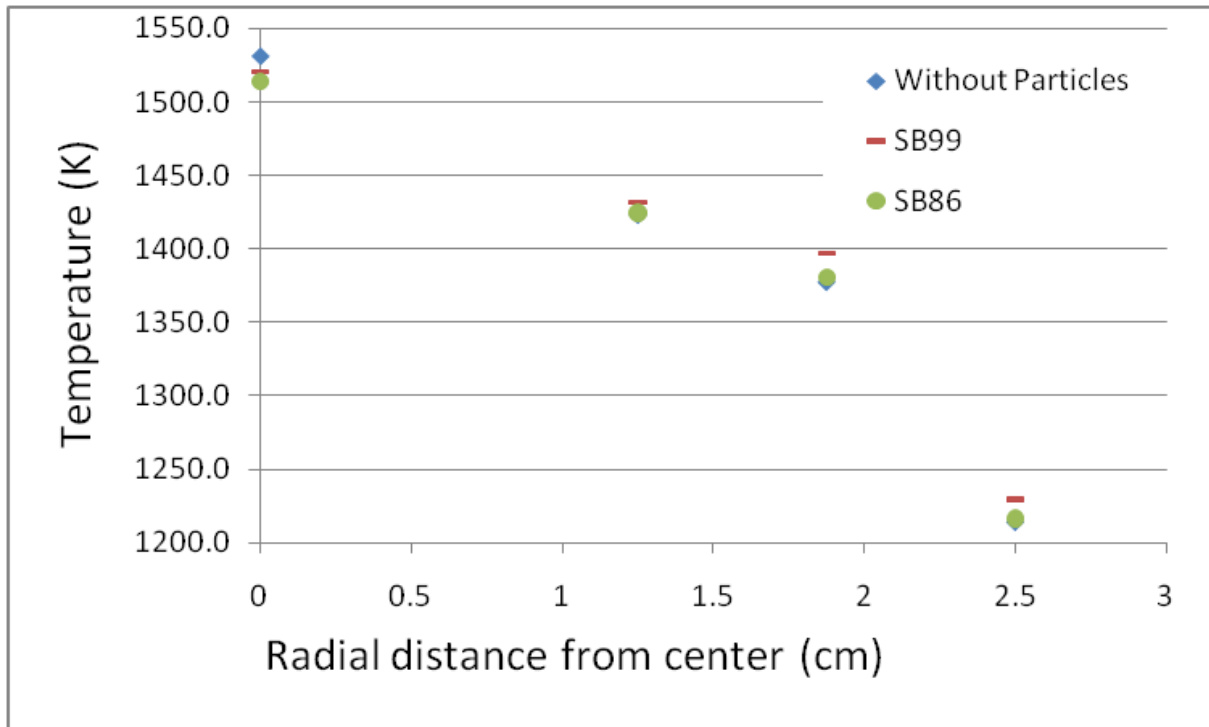


**Figure 3.13: Temperature data for SB99 and SB86, 15in. above the dump plane (Karmakar, 2011).**

From the TGA results, we might also expect the composite nanoparticles BR41-1 and BR41-2 to burn at similar rates to SB86, and we see by comparing Figs. 3.11 and 3.12 that this is true; in fact, at some radial locations the oxide/boron mixtures look slightly better. With the composite REOm-41 mixtures, the increased heat effects can be a result of increased hydrocarbon combustion. The increased temperatures can also stem from increased boron combustion due to the ability of the rare earth oxides to conduct oxygen to the surface of the boron faster than pure boron oxide. The data show that the presence of the rare-earth composites positively affected the heat release, but it is unclear whether the increase was from enhanced ethanol combustion, enhanced boron combustion, or a combination of both.

The temperature data suggest that for the “Sintered” particles the boron combustion rates are slow. This further suggests trouble conducting oxygen to the boron surface because of the more compacted structure that was seen in the SEM and porosimetry data. This result shows that the ignition and burning rates are also dependent on primary particle sizes within the nano-range, because the smaller primary particles of all the other samples had a positive impact on the temperatures. Many other studies have confirmed the dependence of ignition and combustion rates on particle size with micron-sized particles (Yeh et al., 1996; Macek et al., 1969), but Young et al. (2009) proposed that for nanoparticles these rates were insensitive to primary particle size. Our results suggest the trend for micron-sized particles also exists for nanoparticles, in that larger primary particles have slower burning rates.

A summary of the chromatographic results for the sample bombs collected from the combustor exhaust is shown in Tables 3.5-3.7. The analysis is on a dry basis. The species shown here (along with the balance of  $N_2$ ) were the only ones detectable by the thermal conductivity detector of the chromatograph. In all samples, the equivalence ratio (see Eq. 2.8) was 0.69, and



the particle loading was 0.03, which is the particle/fuel ratio on a weight basis. The three cases represent groups of experiments run under different mechanical conditions for the combustor, and because of this fact no comparisons will be made across the cases. In case 1, the original combustion setup was used where the sample collection tube consisted of many unnecessary fittings. In case 2, the collection tube was changed to a single tube with no fittings (Fig 2.1). In case 3, the injection location of the particles was changed from that of the inner air flow to a separate injection location at the centerline of the combustor. Case 3 is the only set of samples that were run at the same conditions as the temperature measurements shown previously, and because of this fact only case 3 data will be compared to the temperature data. The values shown in Tables 3.5-3.7 are given as the average composition  $\pm$  the standard deviation. In all runs, three samples were averaged unless otherwise noted by a subscript.

**Table 3.5: Exhaust Gas Compositions, Case 1.\***

<b>Case 1</b>		<b>Without Particles</b>	<b>SB99</b>	<b>SB95</b>	<b>SB86</b>
run 1	CO <sub>2</sub>	$_{2}3.9 \pm 0.3\%$	$5.6 \pm 0.6\%$	$4.2 \pm 1.3\%$	$_{2}5.3 \pm 0.4\%$
	O <sub>2</sub>	$15.7 \pm 0.5\%$	$13.5 \pm 0.9\%$	$15.3 \pm 1.9\%$	$13.9 \pm 0.6\%$
run 2	CO <sub>2</sub>	$_{2}4.3 \pm 0.1\%$	$4.7 \pm 1.3\%$	$6.5 \pm 0.4\%$	
	O <sub>2</sub>	$15.3 \pm 0.2\%$	$14.5 \pm 2.1\%$	$12.3 \pm 0.4\%$	

\*subscripts refer to the number of injections averaged per run, no subscript means 3 injections.

**Table 3.6: Exhaust Gas Compositions, Case 2.\***

<b>Case 2</b>		<b>Without Particles</b>	<b>SB99</b>	<b>SB95</b>	<b>SB86</b>
run 1	CO <sub>2</sub>	$4.6 \pm 0.6\%$	$7.3 \pm 0.4\%$	$6.7 \pm 0.5\%$	$7.5 \pm 0.2\%$
	O <sub>2</sub>	$14.0 \pm 1.0\%$	$11.1 \pm 0.6\%$	$11.9 \pm 0.6\%$	$11.0 \pm 1.0\%$
run 2	CO <sub>2</sub>	$5.3 \pm 0.3\%$	$7.1 \pm 0.4\%$	$_{2}6.9 \pm 0.2\%$	$7.4 \pm 0.4\%$
	O <sub>2</sub>	$13.8 \pm 0.5\%$	$11.0 \pm 0.8\%$	$11.9 \pm 0.3\%$	$10.5 \pm 0.7\%$

\*subscripts refer to the number of injections averaged per run, no subscript means 3 injections.

**Table 3.7: Exhaust gas compositions, Case 3.\***

<b>Case 3</b>		<b>Without Particles</b>	<b>SB99</b>	<b>SB86</b>	<b>BM</b>	<b>Sintered</b>	<b>BR41-1</b>	<b>BR41-2</b>
run 1	CO <sub>2</sub>	4.1 ± 0.1%	<sub>4</sub> 6.4±0.9%	7.2±0.7%	6.7 ± 0.7%	5.9± 0.7%	6.0 ± 0.9%	6.1±0.6%
	O <sub>2</sub>	14.9 ±0.6%	11.6 ±1.4%	10.3±1.0%	11.2±1.0%	12.5±1.0%	11.2±2.7%	12.5±1.0%
run 2	CO <sub>2</sub>	4.7 ± 1.3%	<sub>2</sub> 7.3±0.2%	7.0 ± 0.6%	5.1 ± 1.4%	3.8 ± 1.2%	6.0 ± 0.1%	<sub>2</sub> 7.2±0.2%
	O <sub>2</sub>	13.9±1.9%	10.0±0.3%	10.4±0.8%	13.6±2.0%	15.4±1.9%	12.5±0.1%	10.0±0.2%
run 3	CO <sub>2</sub>	4.2 ±1.3%	<sub>4</sub> 7.4±0.4%					
	O <sub>2</sub>	15.5 ±2.0%	9.9 ± 0.4%					

\*subscripts refer to the number of injections averaged per run, no subscript means 3 injections.

The theoretical product composition of complete ethanol combustion at an equivalence ratio of 0.69 is 10.15% CO<sub>2</sub> and 6.85% O<sub>2</sub>. The measured amounts of CO<sub>2</sub> presented above are lower than these values, suggesting that ethanol was not completely combusted in the combustion unit or the collected samples were subjected to air dilution before the analysis occurred. Ethanol was tested for and not detected in the collected exhaust samples by GC analysis, implying that if air dilution did not alter the samples, then either all the ethanol was oxidized in the system, or whatever ethanol remained condensed in the collection tube.

As seen in the tables, the amount of measured CO<sub>2</sub> in each sample in case 1 is considerably lower than the other two cases. This difference arises from the mechanical setup, where the unnecessary fittings in the collection tube leaked, allowing outside air to be mixed with the exhaust gas. The differences in cases 2 and 3 could result from the different ways the particles were introduced into the combustor, but the data show little difference anyway, suggesting that the way the particles were introduced had little to no effect on the combustion process.

There was an increase in the CO<sub>2</sub> concentration and a decrease in O<sub>2</sub> for all cases where boron nanoparticles were present. This shows enhanced overall ethanol combustion in the

presence of boron. Cases 1 and 2 show an ~2-3% increase in CO<sub>2</sub> production in the presence of either SB86 or SB99. Therefore it seems that the agglomerate (not the primary particle) size had but little effect on the overall combustion process. Note that their calculated primary particle sizes are almost the same (Table 3.2), while SB86 has a greater pore volume.

In case 3 all the samples are compared, and again it was observed that in the presence of boron nanoparticles, the CO<sub>2</sub> concentration increases. Samples SB99, SB86, and the composite nanoparticle BR41-2 showed the greatest increase in CO<sub>2</sub>. In the case of SB99 and SB86, the more complete combustion of ethanol probably comes from the enhanced heat release upon boron combustion. It is unclear whether SB99 or SB86 had the greater impact on ethanol combustion in this system, but when also taking into account the temperature data (Figures 3.11-3.13), it seems that SB99 produces the same amounts of CO<sub>2</sub> at lower elevations (shorter residence times) than SB86.

In the case of the boron/REOm-41 mixtures, the increased CO<sub>2</sub> can also stem from the rare-earth oxides; Van Devener et al. (2006) showed that CeO<sub>2</sub> can increase CO<sub>2</sub> production in hydrocarbon combustion. The composite nanoparticle with less rare earth oxides, BR41-1, actually gave slightly less CO<sub>2</sub> upon ethanol combustion. Looking at the temperature measurements (Figures 3.11-3.13), both REOm-41/boron mixtures increased the temperatures about the same, but less CO<sub>2</sub> production for BR41-1 implies that some of the combustion enhancement was due to the rare-earth oxide particles improving the conduction of oxygen to the boron surface. The decreased CO<sub>2</sub> production for BR41-1 could be related to less rare-earth oxide or to the further agglomeration (compared to SB99) that was noticed in the SEM images. However, the BR41-2 and BM results did not follow a clear pattern when the runs were repeated, and these were also more agglomerated samples than SB99. Additional runs may be needed to

make a clear determination of the effects of the rare-earth oxides; at this time all that can be said is that the exhaust composition data suggest that BR41-2 and BM were similar in overall combustion behavior to SB99 and SB86, and either synthesis modification can enhance the overall combustion of ethanol to CO<sub>2</sub>. It may therefore be advantageous to substitute some REO for boron, although it is not yet clear what would be the optimal amount. The deviations for BR41-2 between runs 1 and 2 (case 3, Table 3.6) make it difficult to clarify the picture.

There is a clear effect of primary nanoparticle size, in that the “Sintered” particles definitely gave less CO<sub>2</sub>. This confirms the results of the temperature data (Fig. 3.12). This again contradicts the claim by Young et al. (2009), who said that burning rates were independent of particle sizes for nanoparticles. Clearly, the smaller boron primary particles combusted faster and more completely resulting in a greater heat release which enhanced CO<sub>2</sub> production. No previous studies exist that directly show the effects of boron on CO<sub>2</sub> production in hydrocarbon combustion systems.

### **3.3 Final Particle Size, Structure, and Composition**

Diffraction patterns of the final collected (burnt) particles are given in Appendix B. The diffraction patterns for all samples are similar, and because of this only the data for SB99 and “Sintered” are shown in Figure 3.14. There are major peaks at  $2\theta = 28^\circ$  and smaller peaks at  $2\theta = 15^\circ$  and  $40^\circ$  in all cases, and these patterns are consistent with hydrated B<sub>2</sub>O<sub>3</sub> or boric acid (H<sub>3</sub>BO<sub>3</sub>), JCPDS PDF# 30-0019. There were no peaks indicative of elemental B or H<sub>2</sub>BO<sub>3</sub>, showing that the boron nanoparticles were completely oxidized. It has been proposed that H<sub>2</sub>BO<sub>3</sub> is the major product of combustion and that it further reacts upon cooling to B<sub>2</sub>O<sub>3</sub> (Slutskii et al., 1997). Spectroscopic methods employed to measure in-situ compositions of combustion intermediates did not detect H<sub>2</sub>BO<sub>3</sub> as a major product (Karmakar, 2011).

In “wet” atmospheres near room temperature, boron oxide will absorb water from the combustion gases to form the hydrated  $\text{H}_3\text{BO}_3$ . Therefore  $\text{B}_2\text{O}_3$  was the final combustion product.

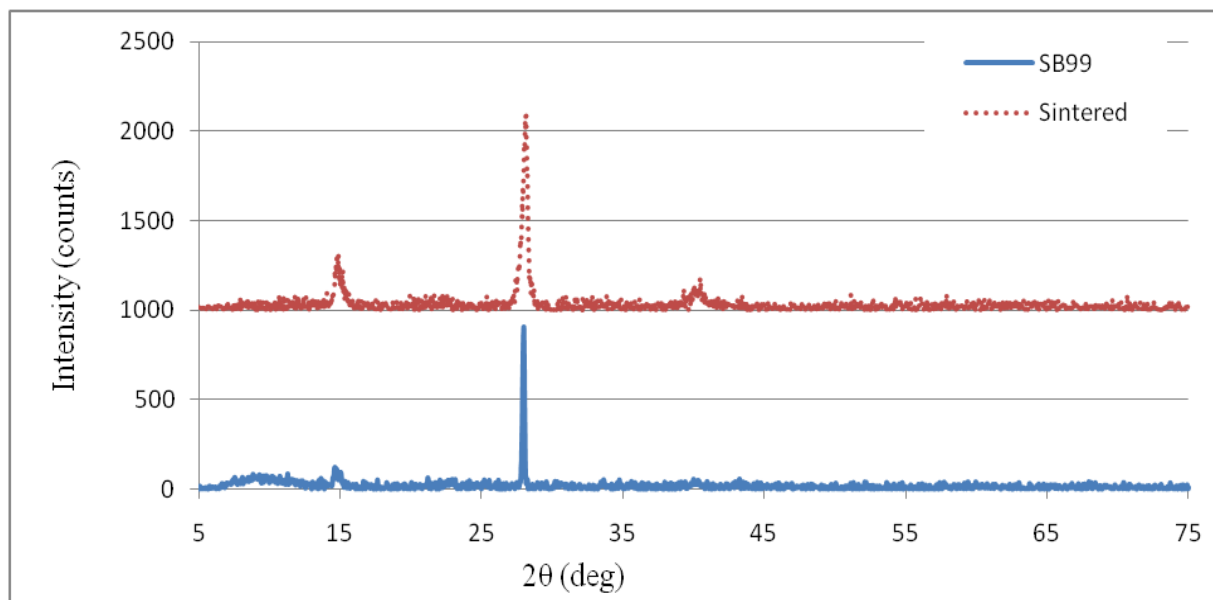


**Figure 3.14: X-Ray diffractogram of burnt SB99 and “Sintered”.**

Particle size estimates on the burnt products were calculated and are presented in Table 3.8. The calculated values are again based on the XRD-visible phase using the Scherrer equation.

**Table 3.8: Burnt particle size estimates from XRD data.**

Sample	SB99	SB86	BM	Sintered	BR41-1	BR41-2
Particle Size (nm)	410	510	220	270	330	240

The crystal sizes are larger for the burnt products than for either the original SB99 or SB86, and this indicates some sintering of the primary crystalline particles upon combustion. The other four cases actually gave smaller crystalline particle sizes than SB99 or SB86, which suggests that their original, in some cases more highly amorphous structures, tended to retard sintering during combustion. Maintaining a smaller particle size upon combustion is important

for the regeneration of the metal fuel additives, because less energy would be needed to break down the used particles back to the nanosize range.

The SEM images of the collected SB99 and SB86 particles are given in Figures 3.15 and 3.16. Both SB99 and SB86 appear to have larger primary particle sizes, consistent with the size estimates in Table 3.8. The particles also appear to form into agglomerates of larger size ( $\sim 0.5$ - $2\ \mu\text{m}$ ) than the feed particles, and their nanostructure appears drastically modified – more regular particle shapes.

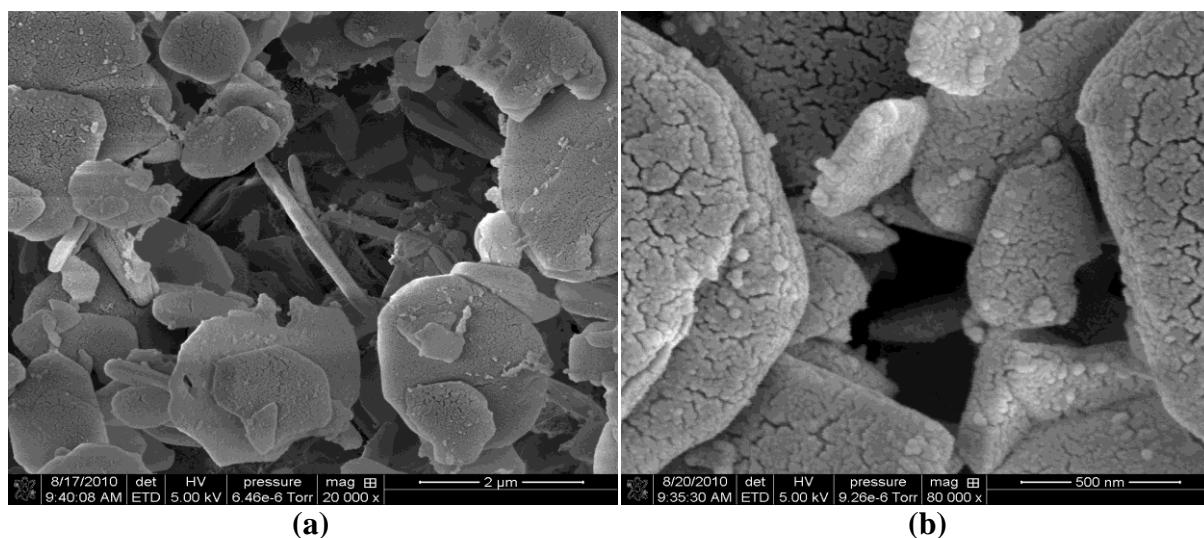


**Figure 3.15: SEM images of collected burnt SB99. Scale is 2  $\mu\text{m}$  (a) and 500 nm (b) (Karmakar, 2011).**

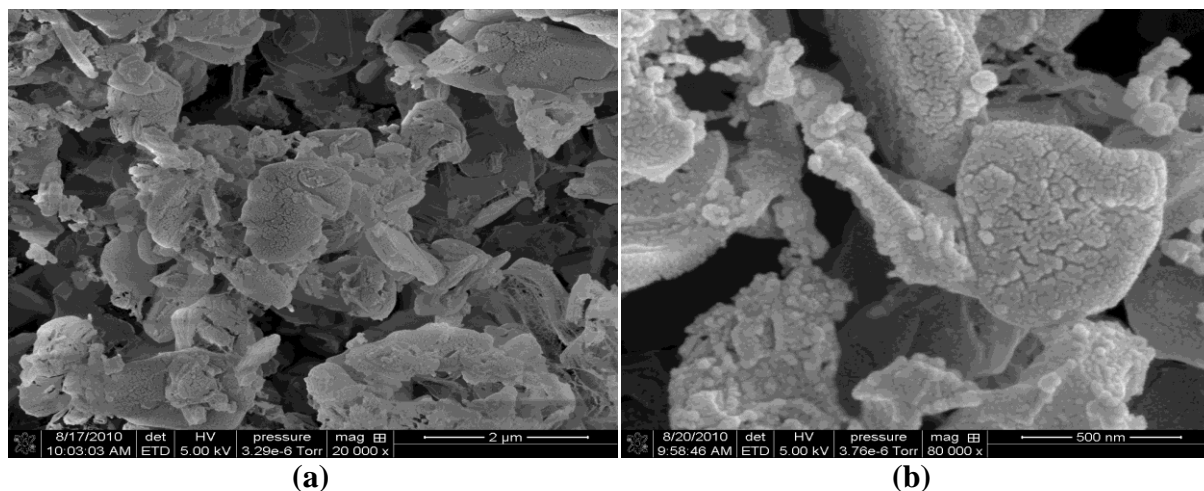


**Figure 3.16: SEM images of collected burnt SB86. Scale is 2  $\mu\text{m}$  (a) and 500 nm (b) (Karmakar, 2011).**

TGA results for the collected particles are presented in Figures 3.17 and 3.18. All data show that the primary reaction between 373 and 473 K is the dehydration of boric acid to boron oxide. Two stages (peaks in the derivative spectrum in Fig. 3.18) of dehydration were detected for all samples, the first centered at approximately 393 K and the second at approximately 448 K. The dehydration reaction weight loss was calculated to be between 38 and 44 wt% for each sample, where the theoretical weight loss for 100% water absorption is 43.6 wt%; therefore, the samples were conclusively shown to be essentially all boric acid, indicating the maximum absorption of water by  $B_2O_3$  upon cooling.

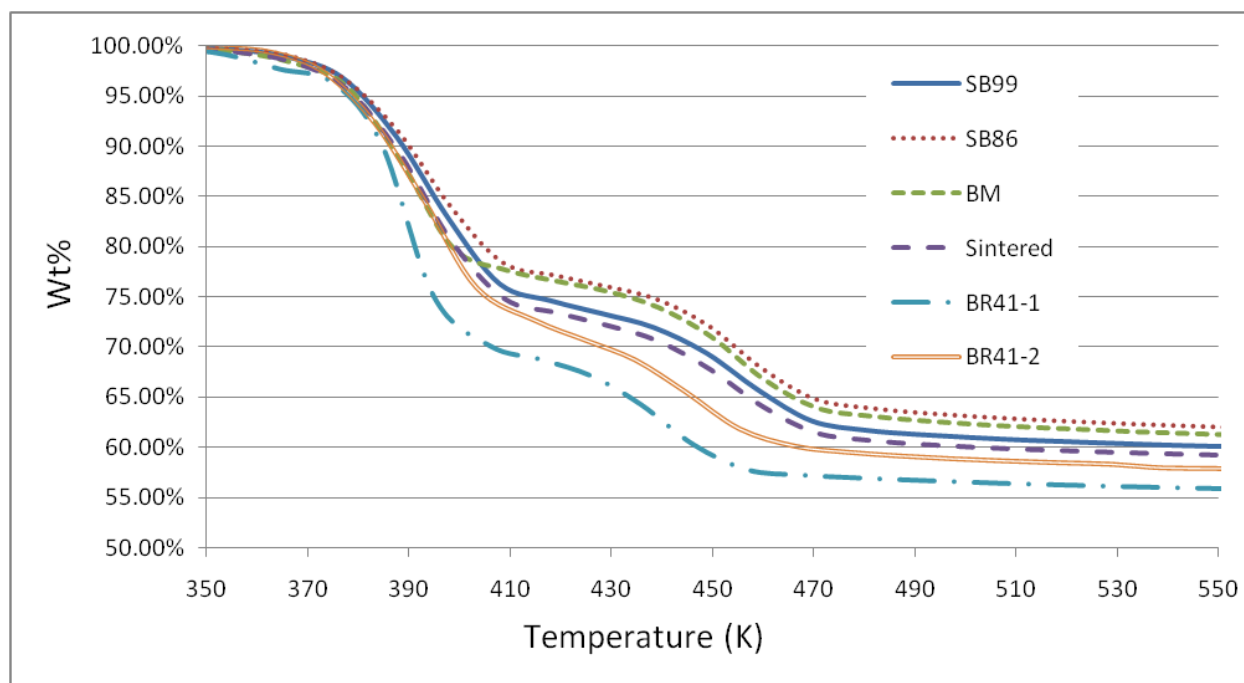


**Figure 3.17: TGA results in air, collected burnt particles.**

It is important to note that no increase in weight occurred throughout these TGA runs, which indicates that no residual elemental boron was present in any of the collected burnt particles; all of the boron present in each sample was fully oxidized.

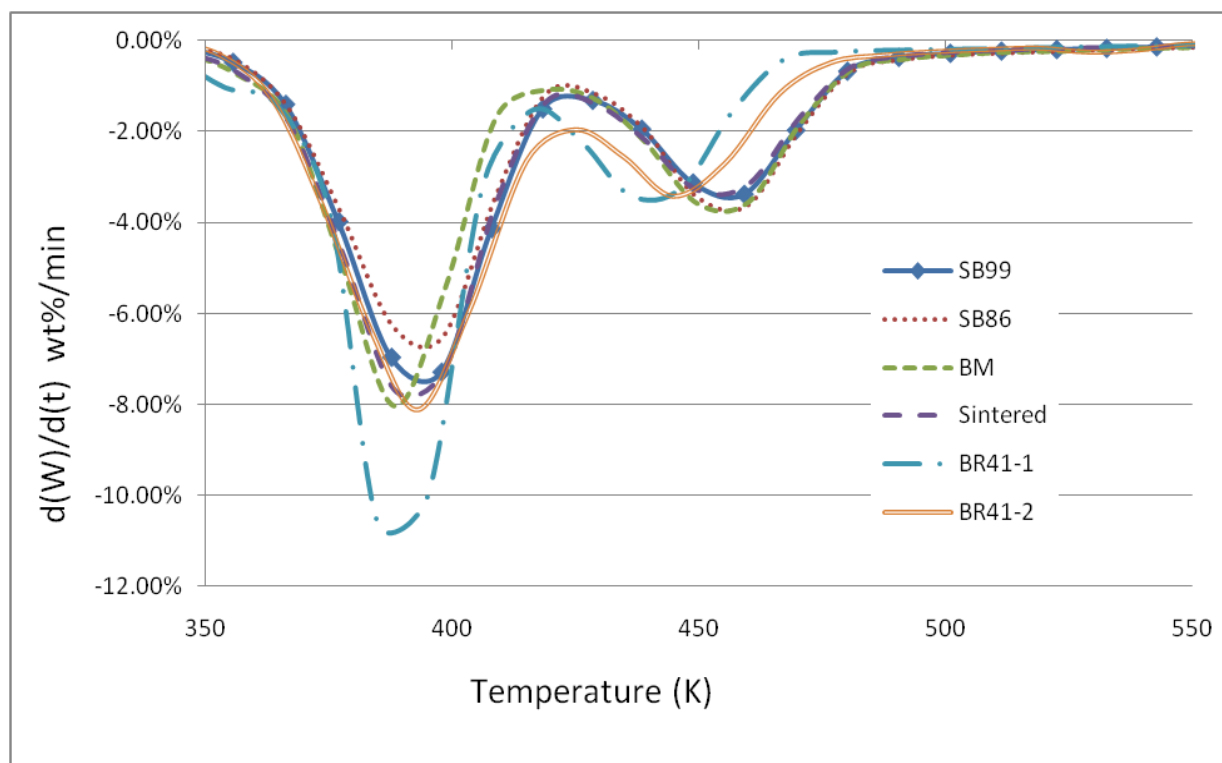


**Figure 3.18: Derivative TGA for collected burnt particles.**



## CHAPTER 4

### CONCLUSIONS

The results show that boron can have a positive impact on ethanol combustion, but its contribution is dependent on both the primary particle and the agglomerate size. The characterization data show two main distinctions between the samples; the first being the primary particle size difference between “Sintered” and all the other samples, and the other being the difference in agglomerate size between SB99 and SB86.

Comparing SB99 (~70 nm) to “Sintered” (~100 nm), the measured temperatures in ethanol combustion were approximately 40 K higher and CO<sub>2</sub> production was 2-3% higher for the smaller particles. Compared to when no particles were present, the smaller SB99 particles showed a 10-15 K increase in temperature and ~3% CO<sub>2</sub> increase, while the larger “Sintered” particles actually decreased the measured temperature near the dump plane of the combustor, while only slightly increasing CO<sub>2</sub> production. The data confirm that within the nano-scale, boron’s effects on ethanol combustion still depend on the primary particle size. The enhancement of ethanol combustion increases as the boron primary particle size decreases.

For commercial boron nanoparticles, the vendor’s particle specifications and the porosimetry data show there is a difference in agglomerate size between SB99 and SB86. Although the exhaust gas analysis shows no difference in overall CO<sub>2</sub> production, the temperature measurements show a delayed heat release in the case of SB86 (larger agglomerates) when compared to SB99. These results show that as agglomeration increases, ignition and combustion times also increase.

The data presented for the rare-earth/boron composites (BR41-1 and BR41-2) show that the addition of rare-earth oxides can also enhance the overall heat release during combustion. Although the data are unclear concerning the optimal composition of such composites, the increased temperatures near the dump plane suggest that even small amounts of rare-earth oxides mixed with boron can positively impact ethanol combustion.

Post-combustion data show that all of the boron particles, independent of their initial morphology, were completely oxidized to hydrated  $B_2O_3$ , and they consisted of a higher fraction of crystals and larger crystallites than the feed particles. Although the modified structure may pose problems in particle regeneration, the work shows that the use of boron nanoparticles and boron/rare earth oxide nanoparticles as combustion additives can increase the actual energy density of bio-fuels.

## REFERENCES

- Aneggi, E., de Leitenburg, C., Dolcetti, G., Trovarelli, A. Catal. Today 114 (2006) 40.
- Aneggi, E., Leitenburg, C., Dolcetti, G., Trovarelli, A. Catalysis Today 138 (2008) 3-10.
- Ashish, J., Anthonysamy, S., Ananthasivan, K., Gupta, G. S. Thermochemica Acta 500 (2010) 63-68.
- Bellott, B.J., Noh, W., Nuzzo, R.G., Girolami, G.S. Chem. Commun. 2009 3214–3215.
- Beloni, E., Hoffman, V. K., Dreizin, E. L. J. of Propulsion and Power 24(6) (2008) 1403-1411.
- Bonnetot, B., Rakic, B., Yuzhakova, T., Guimon, C., Auroux, A. Chem. Mater. 20 (2008) 1585–1596.
- Boichuck, L.V., Shevchuck, V.G., Shvets, A.I. Combustion, Explosion, and Shock Waves 38 (2002) 651-654.
- Brown, R.C., Kolb, C.E., Rabitz, H., Cho, S.Y., Yetter, R.A., Dryer, F.L. International Journal of Chemical Kinetics 23 (1991) 957-970.
- Brown, R.C., Kolb, C.E., Cho, S.Y., Yetter, R.A., Dryer, F.L., Rabitz, H. Intern. J. of Chem. Kinetics. 26 (1994) 319-332.
- Bukatova, G. A., Kuznetsov, S., Gaune-Escard, M. Russian Journal of Electrochem. 43 (2007) 929-935.
- Casey, J.D., Haggerty, J.S. J. Mater. Sci. 22 (1987) 737–744.
- Cordatos, H., Bunluesin, T., Stubenrauch, J., Vohs, J.M., Gorte, R. J. Phys. Chem. 100 (1996) 785.
- Damyanova, S., Bueno, J.M.C. Applied Catalysis A: General 253 (2003) 135-150.
- Decker, B.F., Kasper, J.S. Acta Cryst. 12 (1959) 503-506.
- Demirbas, A. Prog. Energy Combust. Sci. 33 (2007) 1–18.
- Dietz, W.A. J. Gas Chrom. 5 (1967) 68-71.
- Dreizin, E. L., Calcote, H. F. “Chemical and Physical Processes in Combustion”, Eastern States Section Meeting, The Combustion Institute, Pittsburgh, PA, pp. 333 (1995).
- Dreizin, E.L. Progress in Energy and Comb. Sci. 35 (2009) 141–167.
- Gany, A. AIAA 4567, 42<sup>nd</sup> AIAA/ASME/SAE/ASEE Joint Propulsion Conference & Exhibit, Sacramento, California (2006).

Glassman, I., Williams, F. A., Antaki, P. “A physical and chemical interpretation of boron particle combustion”, 20<sup>th</sup> Symposium (Intl.) on Combustion, The Combustion Institute, pp. 2057-2064 (1984).

Goroshin, S., Higgins, A.J., Kamel, M. “Powdered Metals as Fuel for Hypersonic Ramjet” AIAA-2001-3919, 37<sup>th</sup> AIAA/ASME/SAE/ASEE Joint Propulsion Conference and Exhibit Salt Lake City, Utah (2008).

Gurevich, M.A., Kir'yanov, I.M., Ozerov, E.S. Combustion, Explosion, and Shock Waves 5(2) (1969) 150-153.

Kalakota, V. “Sulphur Removal Using Regenerable Sorbents of Rare Earth/Transition Metal Oxides” MS Thesis. Louisiana State University, Baton Rouge, LA, 2008.

Karmakar, S. “Energetic Nanoparticles as Fuel Additive for Enhanced Performance in Propulsion Systems” PhD Thesis. Louisiana State University, Baton Rouge, LA, 2011.

Karmakar, S. Verbal communication. Mech. Eng. PhD Graduate Student (Collaborator). Louisiana State University 2011.

Karmakar, S., Acharya, S., Dooley, K.M. “Combustion of Boron Nanoparticles in Ethanol Spray Flame, Proceedings of 2010 ASME Mechanical Engineering Congress and Expositions, Vancouver, BC, Canada, paper no. IMECE2010-37450 (2010).

King, M. K. Comb. Sci. and Tech. 8 (1974) 255-273.

Kirillova, N.V., Kharlamov, A.I., Loichenko, S.V., Inorganic Materials 36 (2000) 776-782.

Kuo, K.K., Risha, G.A., Evans, B.J., Boyer, E. “Potential Usage of Energetic Nano-sized Powders for Combustion and Rocket Propulsion” Mat. Res. Soc. Symp. Proc. Boston, Massachusetts (2003).

Li, S. C. and Williams, F. A. “An Investigation of Combustion of Boron Suspensions”, 22nd Symposium (Intl.) on Combustion, The Combustion Institute, pp. 1951-1960 (1988).

Liotta, L.F., Deganello, G., Sannino, D., Gaudino, M.C., Ciambelli, P., Gialanelli, S. Applied Catalysis A: General 229 (2002) 217-227.

Macek, A., Semple, J. M. Comb. Sci. and Tech. 1 (1969) 181-191.

Masui, T., Hirai, H., Hamada, R., Imanaka, N., Adachi, G., Sakata, T., Mori, H. J. Mater. Chem. 13 (2003) 622-627.

Matovnikov, A., Urbanovich, V., Chukina, T., Sidorov, A., Novikov, V. Inorganic Materials 45 (2009) 366-368.

Mehendale, B., Shende, R., Subramanian, S., Gangopadhyay, S., Redner, P., Kapoor, D. Journal of Energetic Materials 24 (2006) 341-60.

- Mohammad Sharifi, E., Karimzadeh, F., Enayati, M.H. Journal of Alloys and Compounds 482 (2009) 110–113.
- Mohan, G., Williams, F. A. AIAA Journal 10(6) (1972) 776-783.
- Mori, T., Zhang, F., Tanaka, T. J. Phys. Condens. Matter 13 (2001) L423–L430.
- Mota, J.M., Martinez, M.A., Velasco, F., Criado, A.J. Ceramics International 30 (2004) 301–306.
- Oliker, V. E., Sirovatka, V.L., Gridasova, T.I., Timofeeva, I.I., Bykov, A.I. Powder Metallurgy and Metal Ceramics 47 (2008) 9-10.
- Rang, H., Kahn, J. Proc. Estonian Acad. Sci. Chem. 52 (2003) 130–142.
- Resende, V.G., Grave, E., Costa, G.M., Janssens, J. Journal of Alloys and Compounds 440 (2007) 236-247.
- Rosenband, V., Natan, B., Gany, A. Journal of Propulsion and Power 11(6) (1995) 1125-1131.
- Schoenitz, M., Ward, S., Dreizin, E.L. Proceedings of the Combustion Institute 30 (2005) 2071-2078.
- Shen, J., Li, Z., Wang, Q., Chen, Y. Journal of Material Science 32 (1994) 749-753.
- Shevchuk, V.G., Zolotko, A.N., Polishchuk, D. I. Combustion Explosion and Shock Waves 11(2) (1975) 189–192.
- Si, P. Z., Zhang, M, You, C. Y., Geng, D. Y., Du, J. H., Zhao, X. G., Ma, X. L., Zhang, Z .D. J. Mater. Sci. 38 (2008) 689–692.
- Singhal, A., Skandan, G., Wang, A., Glumac, N., Kear, B.H., Hunt, R.D. Nanostructured Materials 11(4) (1999) 545-552.
- Slutskii, V. G., Severin, E. S., Polenov L. A. Russian Journal of Physical Chemistry B 1(6) (2007) 549–552.
- Sullivan, K., Young, G., and Zachariah, M.R. Combustion and Flame 156(2) (2009) 302-309.
- Takeda, H., Kuno, H., Adachi, K. J. Am. Ceram. Soc. 91 (2008) 2897–2902.
- Tobo, A., Yamauchi, H., Kishi, E., Sakata, M., Ishimoto, K., Ohoyama, K., Onodera, H., Yamaguchi, Y.A. J. Physic.: Condensed Matter 15 (2003) S2141-S2144.
- Trovaletti, A., de Leitenburg, C., Boaro, M., Dolcetti G., Catal. Today 50 (1999) 353.
- Trunov, M., Hoffman, V., Schoenitz, M., Dreizin, E. Journal of Propulsion and Power 24(2) (2008) 184-191.

- Ulas, A., Kuo, K. K., Gotzmer, C. Combustion and Flame 127 (2001) 1935–1957.
- Van Devener, B., Anderson, S.L. Energy and Fuels 20 (2006) 1886-1894.
- Van Devener, B., Paulo, J., Anderson, S. J. Mater. Res. 24(11) (2009) 3462-3464.
- Van Devener, B.V., Perez, J.P.L., Jankovich, J., Anderson, S.L. Energy and Fuels 23 (2009) 6111-6120.
- Vlasse, M., Boiret, M., Naslain, R., Kasper, J.S., Ploog, K. C.R. Seances Acad. Sci. Ser. C 287 (1978) 27-30.
- [www.sbboron.com/pdf/SBBoron86specsheat.pdf](http://www.sbboron.com/pdf/SBBoron86specsheat.pdf). SB Boron Corp. Spec Sheet.
- Xu, T.T., Zheng, J.G. Wu, N. Nicholls, A.W. Roth, J.R., Dikin, A.D., Ruoff, R.S. Nano Letters 4(5) (2004) 963-968.
- Yamaguchi, Y. J. Phys. Condens. Matter 15 (2003) S2141–S2144.
- Yan, S.J., Xue, D.S. J. Mater. Sci. 43 (2008) 771–774.
- Yeh, C.L., Kuo, K.K. Prog. Energy Combust. Sci. 22 (1996) 511-541.
- Yetter, R. A., Rabitz, H., Dryer, F. L, Brown, R. C., Kolb, C. E. Combustion and Flame. 83 (1991) 43-62.
- Yetter R.A., Risha G.A., Son, S.F. Proc. of Comb. Inst. 32 (2009) 1819-1838.
- Young, G., Sullivan, K., Zachariah, M., and Yu, K. Combustion and Flame 156 (2009) 322-333.
- Yuzhakova, T., Rakic', V., Guimon, C., Auroux, A. Chem. Mater. 19 (2007) 2970-2981.
- Zhang, M., Yuan, L., Wang, X., Fan, H., Wang, X., Wu, X., Wang, H., Qian, Y. Journal of Solid State Chemistry 181 (2008) 294–297.
- Zhao, S., Gorte, R.S. Applied Catalysis A: General 277 (2004) 129-136.
- Zolotko, A.N., Klyachko, L.A., Kopeika, K.M., Polishchuk, D.I., Shevchuk, V.G. Combustion Explosion and Shock Waves 13 (1977) 31–36.

## APPENDIX A

### GAS CHROMATOGRAPHY (GC) DETAILS

**Table A.1: GC Settings:** Alltech CTR1 column, 1/8" inner column packed with a porous polymer mixture, and 1/4" outer column packed with activated molecular sieve.

Parameter	Setting
Carrier Gas	He
Column Pressure	26.5 psi
Column Flow Rate	62 mL/min
Reference Flow Rate	62 mL/min
Initial Oven Temperature	27°C
Initial Hold Time	4 min
Ramp Rate	20°C/min
Final Temperature	130°C
Final Hold Time	4 min
Total Run Time	21.15 min
Detector Temperature	150°C
Detector Filament Temperature	250°C
Column Split Ratio: Inner/Outer	0.39

**Table A.2: Retention Times:** The following were determined by injecting standards into the column and measuring elution times.

Species, Column	Retention Time (min)
Air/CO, inner	0.7-0.8
CH <sub>4</sub> , inner	0.8-0.9
CO <sub>2</sub> , inner	1.6-2.0
C <sub>2</sub> 's (ethane and ethylene), inner	2
O <sub>2</sub> , outer	2.6-2.7
N <sub>2</sub> , outer	3.9
CH <sub>4</sub> , outer	5.7-5.8
CO, outer	7.3-7.7
CO <sub>2</sub> , outer	9.3
H <sub>2</sub> O, inner	> 11
*Inner and Outer refer to the inner and outer columns.	

## APPENDIX B

### XRD DIFFRACTOGRAMS

**Feed particles:** The following XRDs were collected using the Rigaku Mini-Flex diffractometer at the LSU Materials Characterization Center, using the standard bulk sample mount. The scan was from  $2\theta = 5$  to  $75^\circ$  at a scan rate of  $1^\circ/\text{min}$  and a  $0.02^\circ$  step size. NIST standard  $\alpha$ -alumina was also run and compared to its known diffraction pattern (JCPDS # 10-0173) in order to correct the  $2\theta$  values. From this comparison an equation to correct the  $2\theta$  values of the unknowns was regressed, giving the following:

$$2\theta \text{ shift} = -3 \times 10^{-7} x^3 + 0.0002 x^2 + 0.0099 x - 2.2008$$

where  $x$  is the original  $2\theta$  value given by the Rigaku software. Only corrected diffractograms are shown below and in the thesis.

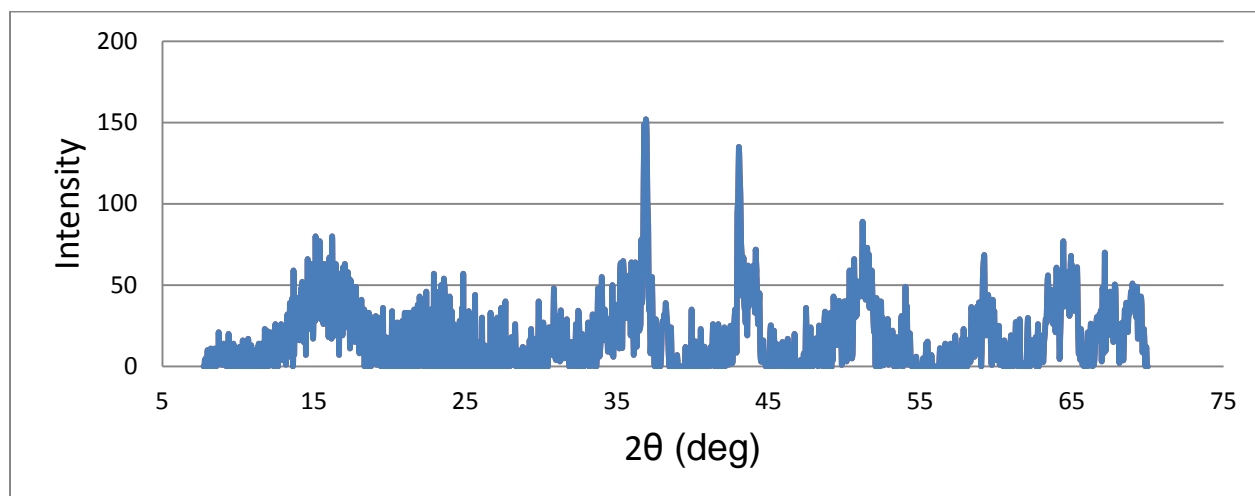


**Figure A.1: X-Ray Diffractogram of SB99**

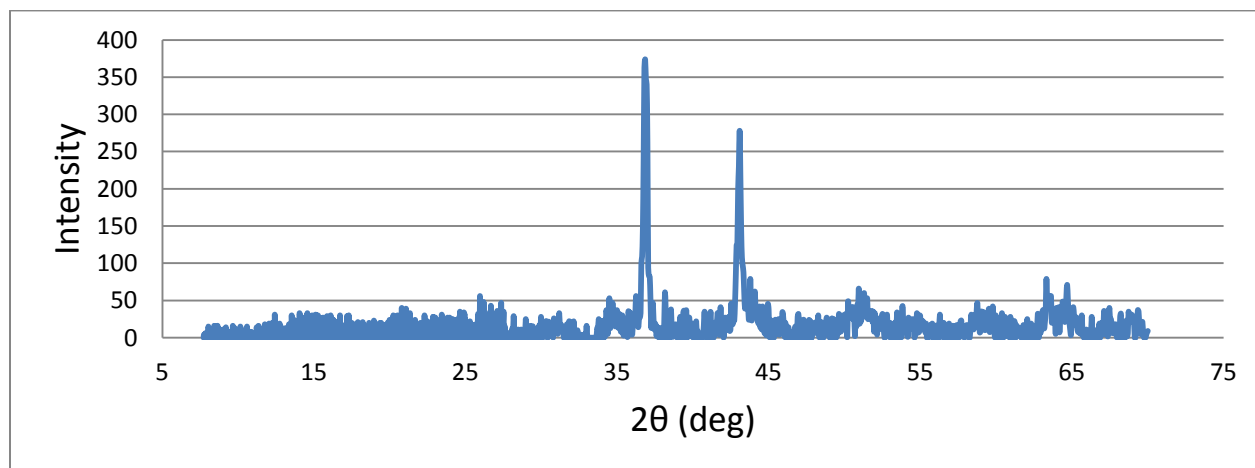


**Figure A.2: X-Ray Diffractogram of SB86**



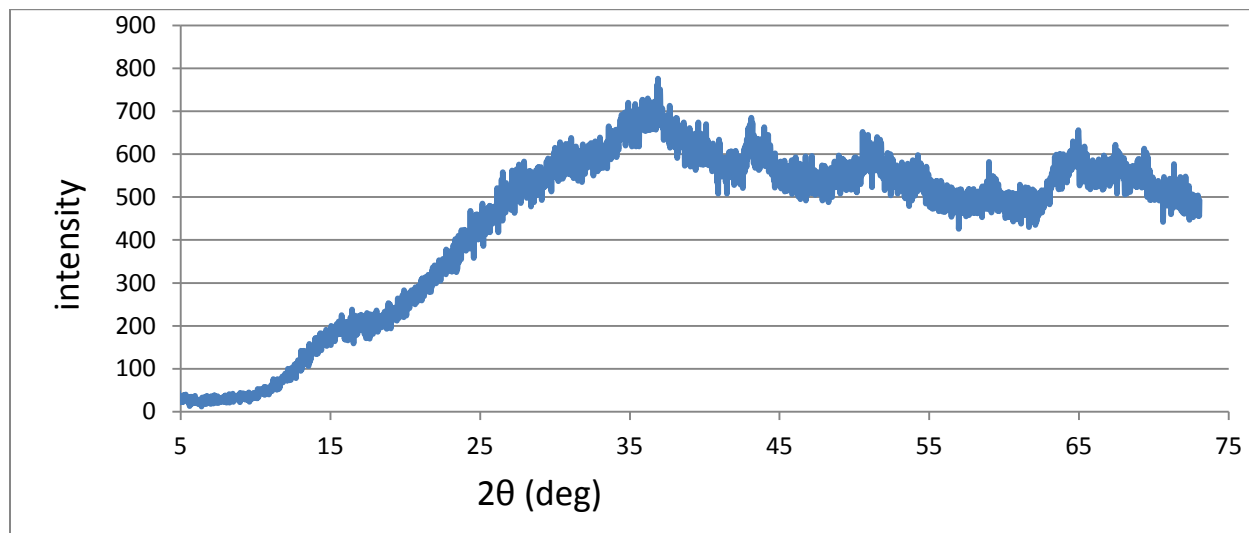


**Figure A.3: X-Ray Diffractogram of BM (ball milled)**

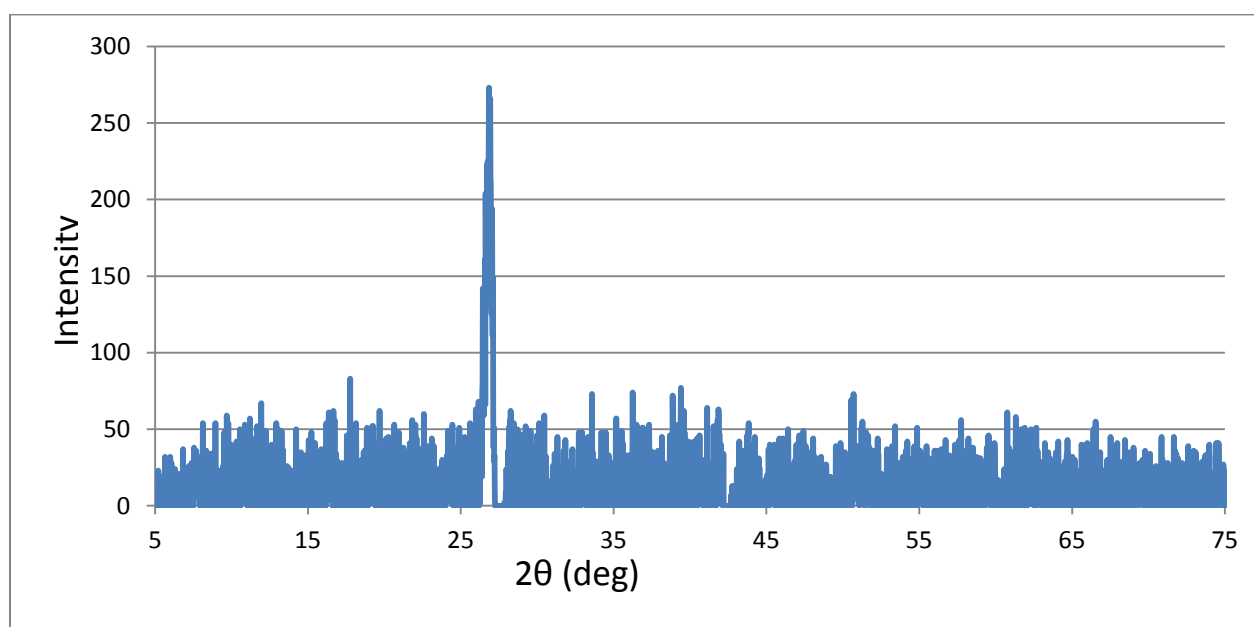


**Figure A.4: X-Ray Diffractogram of “Sintered”**

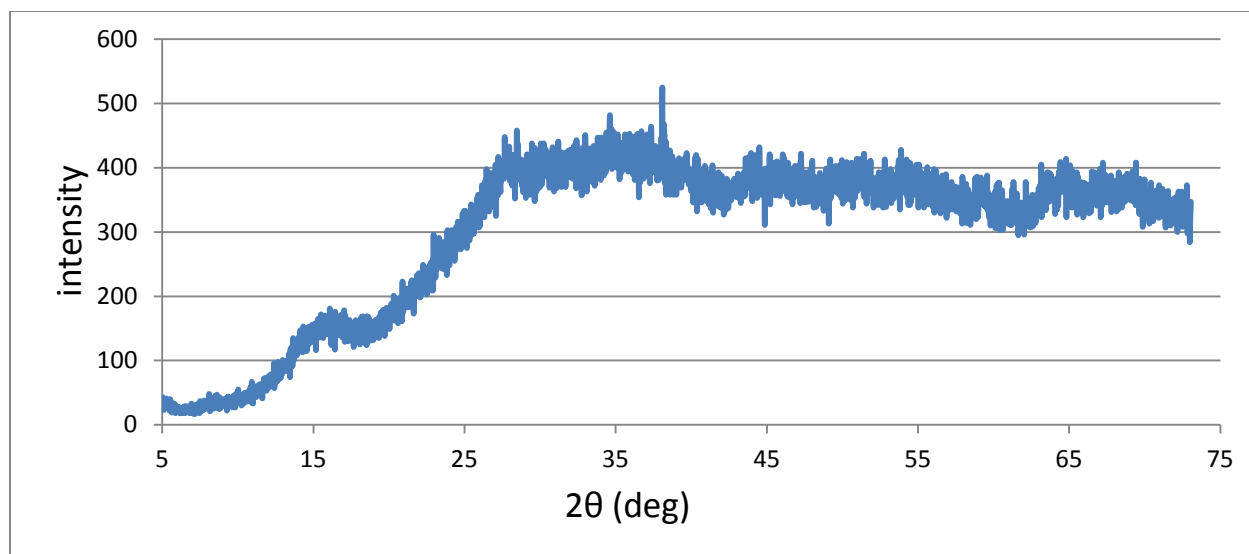


**Figure A.5: X-Ray Diffractogram of BR41-2 (95/5 mix)**

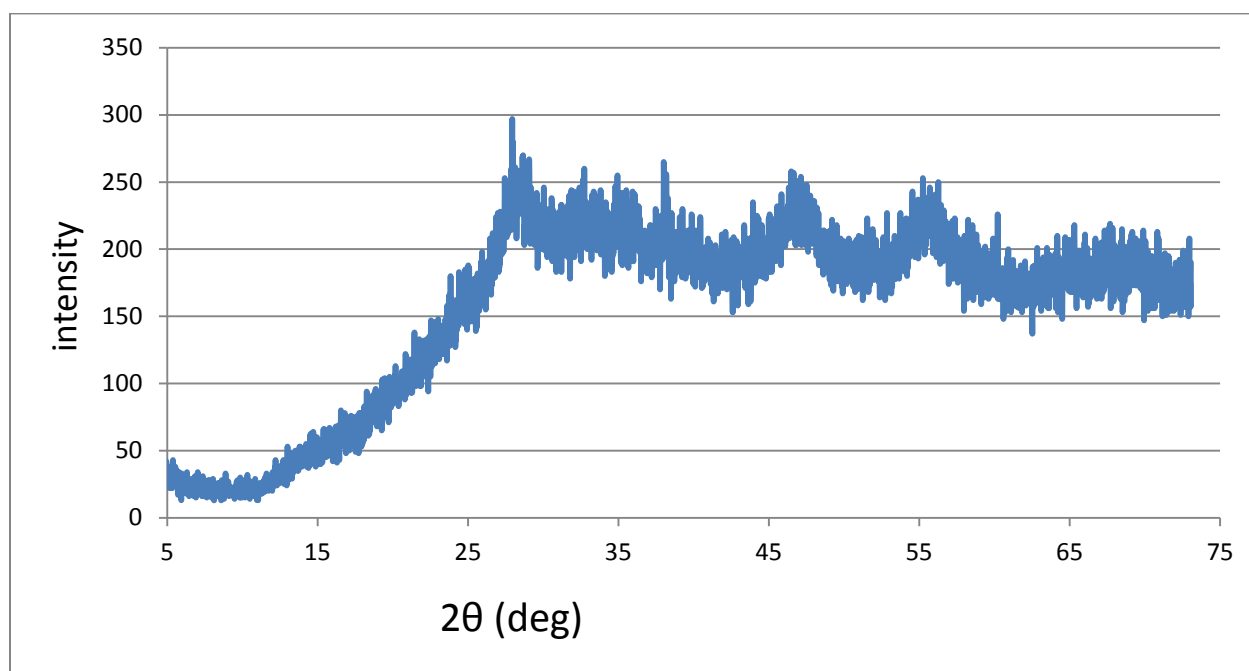


**Figure A.6: X-Ray Diffractogram of BR41-2 (80/20 mix)**

The following diffractograms were collected using the Powder Diffraction Beamline at CAMD (LSU Center for Advanced Microstructures and Devices), using the standard bulk sample holder, at a scan rate of 0.1°/min and a scan rate of 0.02°. Samples were scanned at various  $2\theta$  ranges from 5-75°.

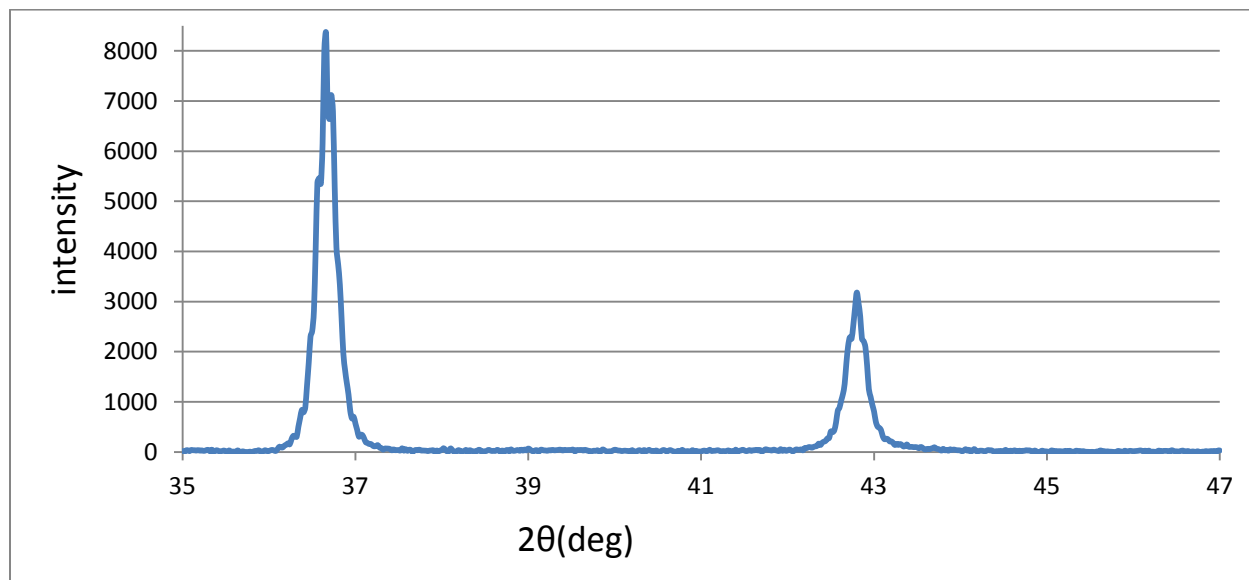


**Figure A.7: X-Ray Diffractogram of SB99 (CAMD)**

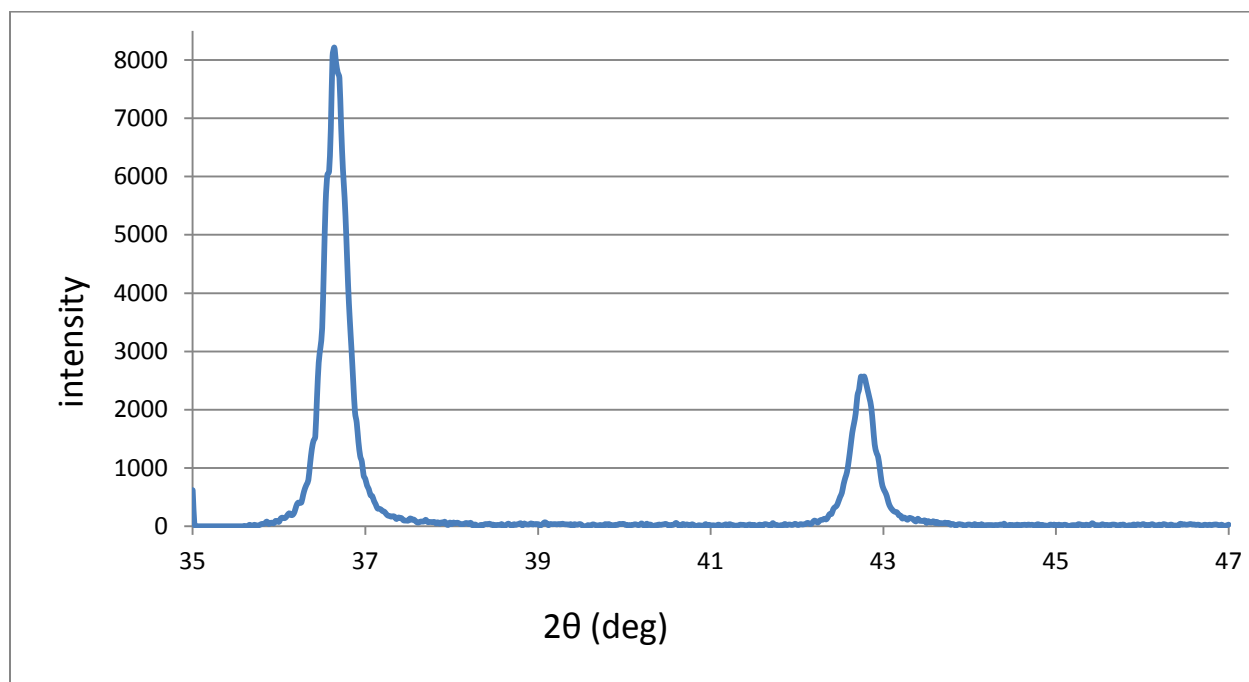


**Figure A.8: X-Ray Diffractogram of SB86 (CAMD)**

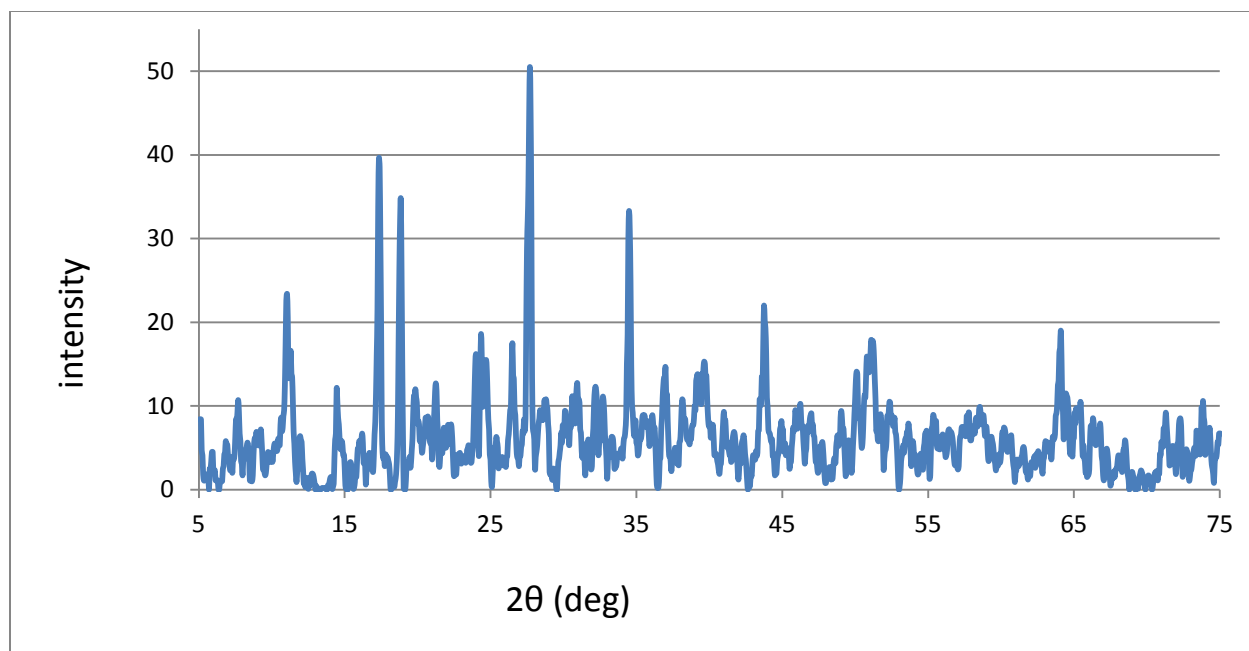


**Figure A.9: X-Ray Diffractogram of BR41-1 (95-5 Mix) (CAMD)**

**Burnt Particles:** The following diffractograms were collected using the Rigaku Mini-Flex diffractometer, at the LSU Materials Characterization Center. The samples were mounted on double sided tape. No correction was necessary based on an  $\alpha$ -alumina standard compared to its known diffractogram (JCPDS # 10-0173). Samples were scanned from  $2\theta = 5-75^\circ$  at a scan rate of  $1^\circ/\text{min}$  and a step size of  $0.02^\circ$ .

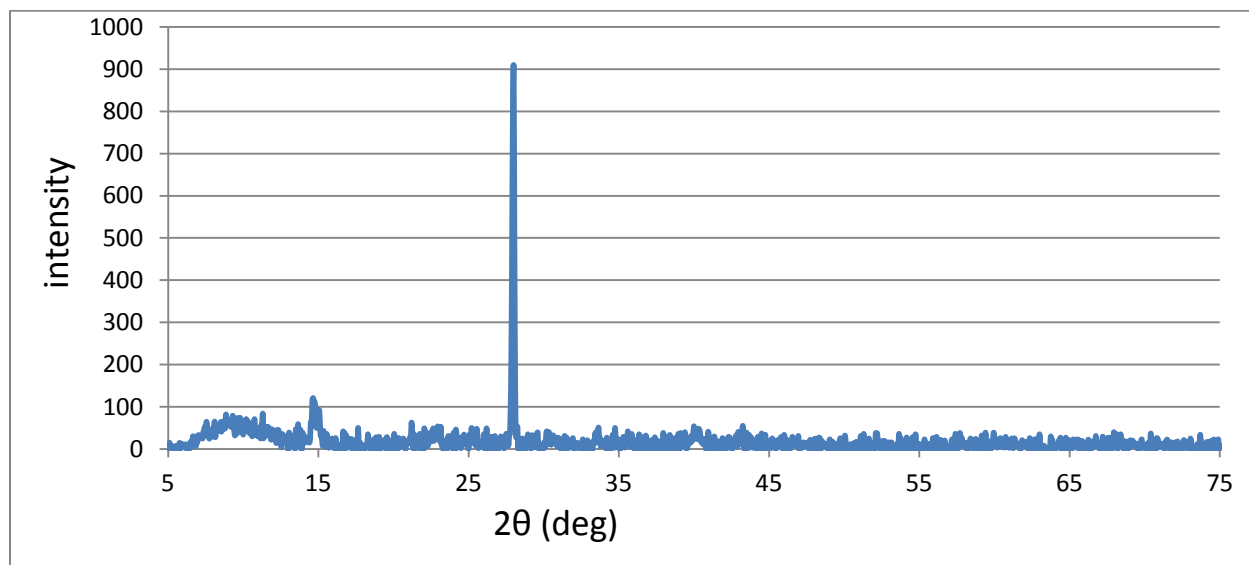


**Figure A.10: X-Ray Diffractogram of SB99 Burnt**

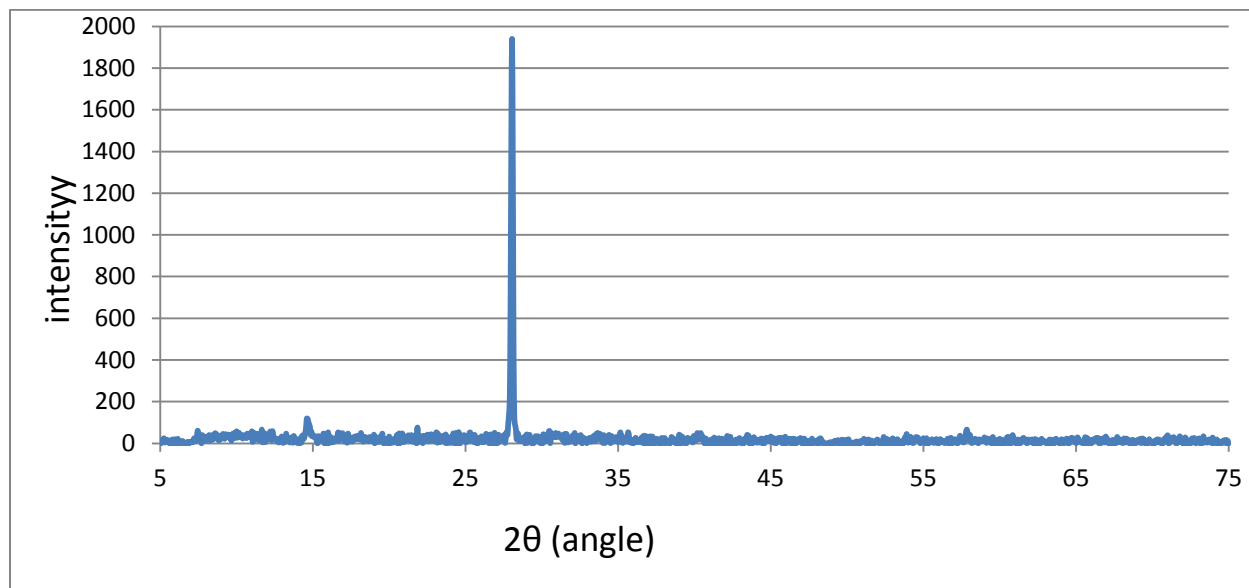


**Figure A.11: X-Ray Diffractogram of SB86 Burnt**

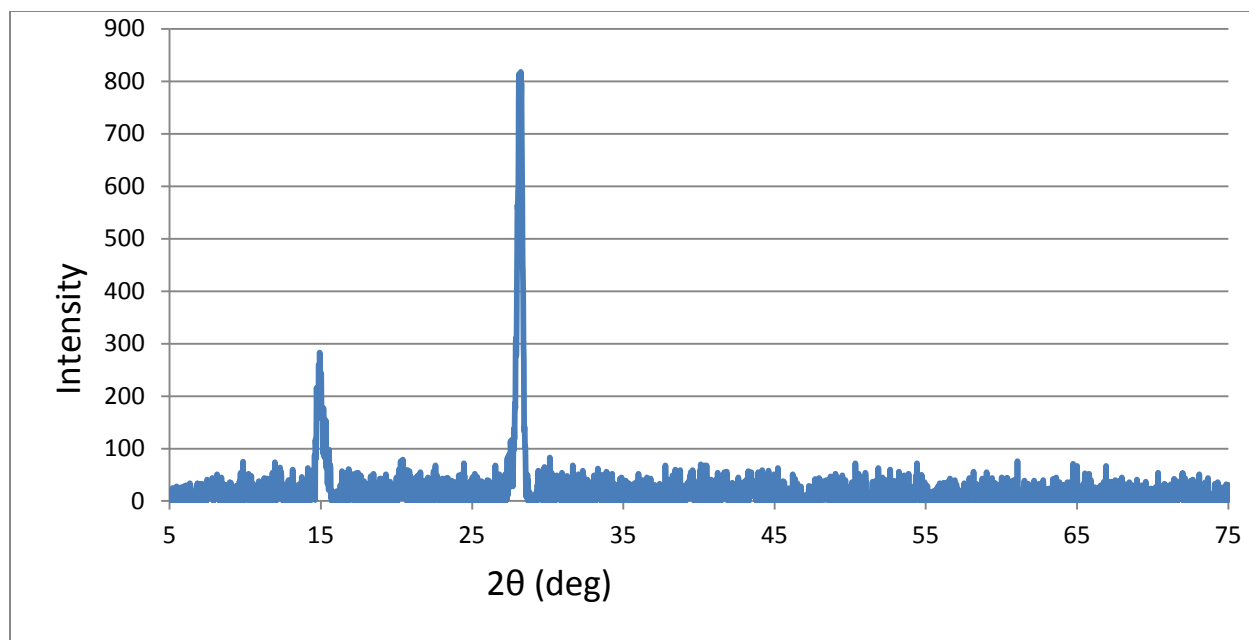


**Figure A.12: X-Ray Diffractogram of BM Burnt**

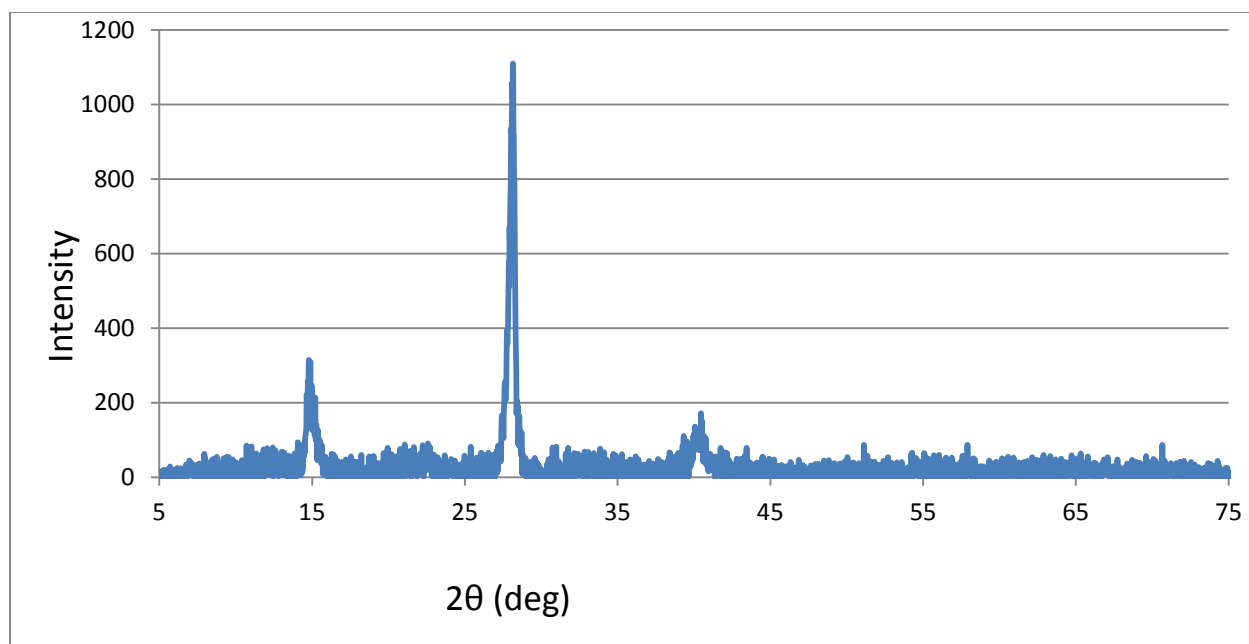


**Figure A.13: X-Ray Diffractogram of Sintered Burnt**

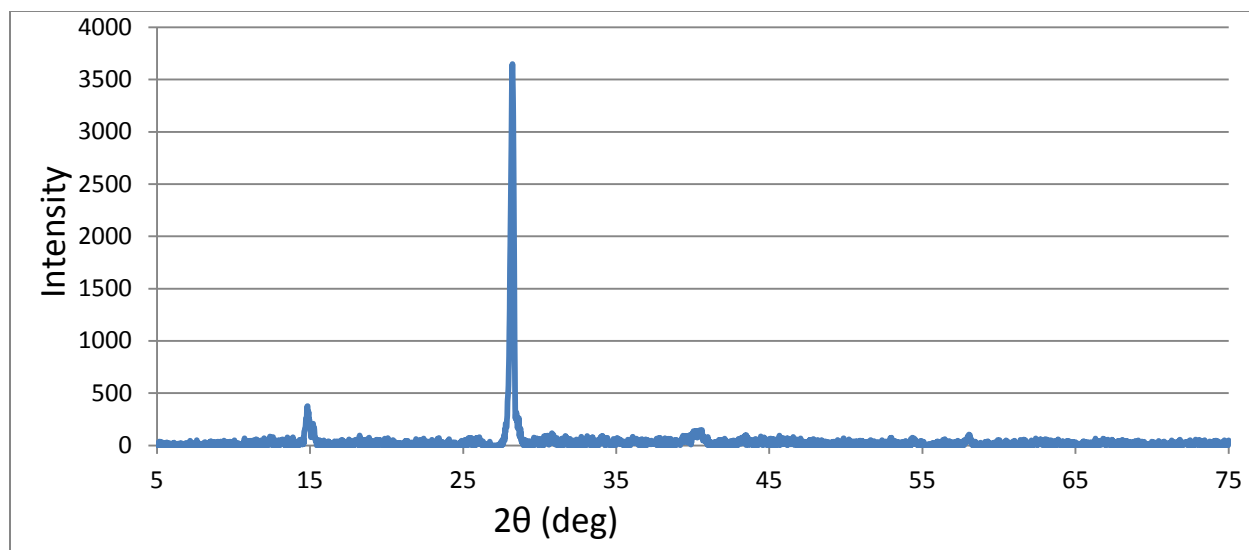


**Figure A.14: X-Ray Diffractogram of BR41-1 Burnt (95-5 mix)**

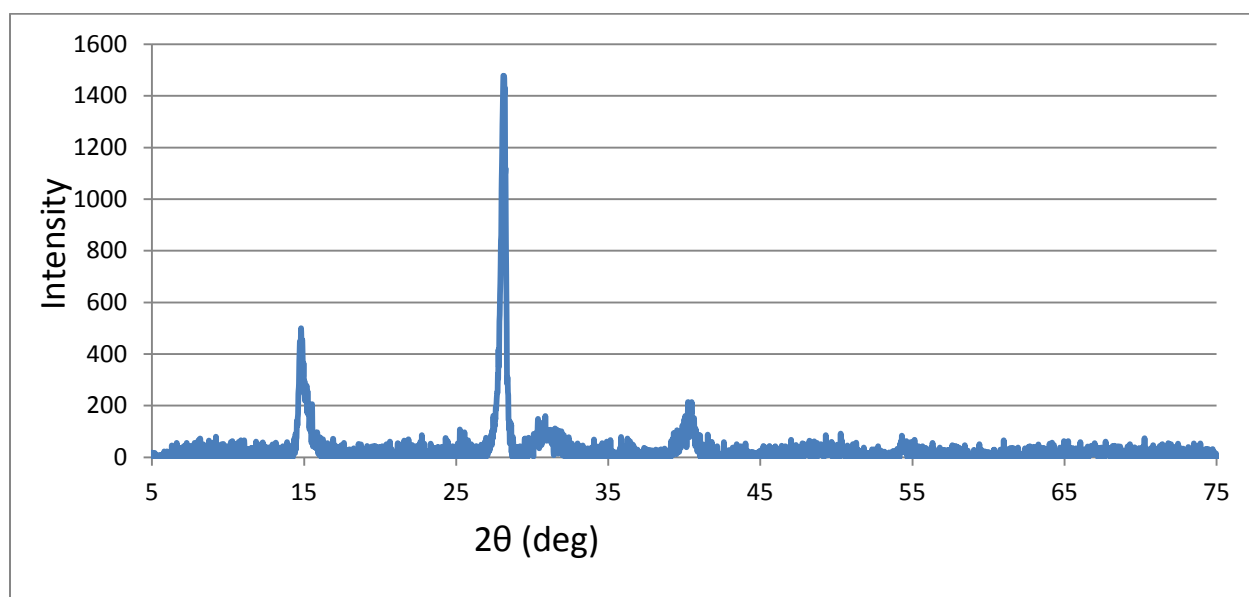


**Figure A.15: X-Ray Diffractogram of BR41-2 Burnt (80-20 mix)**

## **VITA**

Jacob Hanberry was born in 1985 to Joel and Elaine Hanberry in Raceland, LA. He finished his high school education at South Lafourche High School in Galliano, Louisiana, and went on to complete a Bachelor of Science in Chemistry at Millsaps College in December 2008. He entered the graduate program at Louisiana State University in August 2009, and this thesis completes his requirements to receive a Master of Science in Chemical Engineering.